SN 2016esw: a luminous Type II supernova observed within the first day after the explosion

Thomas de Jaeger,[1]⋆ Lluís Galbany,[2]⋆ Claudia P. Gutiérrez,[3]⋆ Alexei V. Filippenko,[1,4]†
WeiKang Zheng,[1] Thomas G. Brink,[1] Ryan J. Foley,[5] Sebastian F. Sánchez,[6]
Sanyum Channa,[1] Maxime de Kouchkovsky,[1] Goni Halevi,[1,7] Charles D. Kilpatrick,[5]
Sahana Kumar,[1,8] Jeffrey Molloy,[1] Yen-Chen Pan,[5] Timothy W. Ross,[1] Isaac Shivvers,[1]
Matthew R. Siebert,[5] Benjamin Stahl,[1] Samantha Stegman,[1] and Sameen Yunus[1]

[1]*Department of Astronomy, University of California, Berkeley, CA 94720-3411, USA*
[2]*PITT PACC, Department of Physics and Astronomy, University of Pittsburgh, Pittsburgh, PA 15260, USA*
[3]*University of Southampton, School of Physics and Astronomy, Southampton, SO17 1BJ, UK*
[4]*Miller Institute for Basic Research in Science, University of California, Berkeley, CA 94720, USA*
[5]*Department of Astronomy and Astrophysics, University of California, Santa Cruz, CA 95064, USA*
[6]*Instituto de Astronomía, Universidad Nacional Autonóma de México, A.P. 70-264, 04510 México D.F., Mexico*
[7]*Department of Astrophysical Sciences, Princeton University, Princeton, NJ 08544, USA*
[8]*Department of Physics and Astronomy, Florida State University, Tallahassee, FL 32306, USA*

ABSTRACT

We present photometry, spectroscopy, and host-galaxy integral-field spectroscopy of the Type II supernova (SN II) 2016esw in CGCG 229-009 from the first day after the explosion up to 120 d. Its light-curve shape is similar to that of a typical SN II; however, SN 2016esw is near the high-luminosity end of the SN II distribution, with a peak of $M_V^{max} = -18.36$ mag. The V-band light curve exhibits a long recombination phase for a SN II (similar to the long-lived plateau of SN 2004et). Considering the well-known relation between the luminosity and the plateau decline rate, SN 2016esw should have a V-band slope of $\sim$2.10 mag (100 d)$^{-1}$; however, SN 2016esw has a substantially flatter plateau with a slope of 1.01 ± 0.26 mag (100 d)$^{-1}$, perhaps indicating that interacting Type II supernovae are not useful for cosmology. At 19.5 d post-explosion, the spectrum presents a boxy Hα emission line with flat absorption profiles, suggesting interaction between the ejecta and circumstellar matter. Finally, based on the spectral properties, SN 2016esw shows similarities with the luminous and interacting SN 2007pk at early epochs, particularly in terms of observable line features and their evolution.

Key words: supernovae: general – supernovae: individual: 2016esw.

1 INTRODUCTION

Type II supernovae (hereafter SNe II) are characterized by strong hydrogen Balmer lines in their spectra. Their progenitors are initially (zero-age main sequence; ZAMS) massive stars ($M_{ZAMS} \not\gtrsim$ 8 M$_\odot$; see Smartt et al. 2009 for a review, and references therein) that did not shed their outer envelope prior to exploding.

SNe II exhibit a large range of observed photometric and spectroscopic properties and can be further separated into several subclassifications (see Filippenko 1997, and references therein). Historically,

a first subclassification based on the light-curve morphologies was made: SNe IIP, which exhibit a long-duration plateau ($\lesssim$100 d) of roughly constant luminosity, and SNe IIL, which show a faster declining light curve (Barbon, Ciatti & Rosino 1979). However, recent studies on large data sets (Anderson et al. 2014; Sanders et al. 2015; Valenti et al. 2016; Galbany et al. 2016a, also see Rubin et al. 2016) do not favour such bimodality in the diversity, instead suggesting that the SN IIP and SN IIL families form a continuous class. Therefore, henceforth we simply refer to these two subgroups as SNe II.

Based on the spectroscopic properties, two other subgroups were proposed: SNe IIb, which evolve spectroscopically from SNe II at early times to H-deficient a few weeks to a month past maximum brightness (Woosley et al. 1987; Filippenko 1988; Filippenko,

⋆ E-mail: tdejaeger@berkeley.edu (TD) lluisgalbany@gmail.com (LG) klaudisp@gmail.com (CG)
† Miller Senior Fellow.

Matheson & Ho 1993), and SNe IIn, which have relatively narrow H I emission lines owing to interaction between the ejecta and dense circumstellar matter (CSM; Chevalier 1981; Fransson 1982; Schlegel 1990; Filippenko 1991). Note that in this work, these last two subgroups are not considered in our photometric or spectroscopic analysis, as their characteristics differ from those of the SN II family (SNe IIP and SNe IIL) to which our object belongs.

Thanks to direct progenitor detections (Van Dyk, Li & Filippenko 2003; Smartt et al. 2009; Smartt 2009) and hydrodynamical models (Grassberg, Imshennik & Nadyozhin 1971; Falk & Arnett 1977; Chevalier 1976), it is known that most SN II progenitors are red supergiant stars (RSGs; 8–16 $M_\odot$). Nevertheless, we see a great variety of SNe II in the Universe (e.g. Filippenko 1991; Hamuy 2003; Anderson et al. 2014; Gutiérrez et al. 2017). This diversity results from differences among progenitors and explosion mechanisms, such as the mass of the H envelope, the radius, the metallicity, the explosion energy, the mass-loss, and the amount and nature of interaction with CSM. For example, faster declining SN II progenitor (historically SNe IIL) may have greater ZAMS masses (Elias-Rosa et al. 2010, 2011) and smaller H envelopes (Popov 1993), or be RSGs surrounded by dense CSM (Morozova, Piro & Valenti 2017b).

As SNe II have also been established to be useful independent distance indicators (Hamuy & Pinto 2002), a better understanding of SN II diversity will be useful not only for our knowledge of SN II properties but also for reducing the scatter in the Hubble diagram, and thus obtaining tighter constraints on the cosmological parameters (de Jaeger et al. 2017a,b).

SN 2016esw provides a good opportunity to explore the zoo of SNe II owing to the acquisition of well-sampled data starting less than 1 d after the explosion. In this paper, we present optical photometry and spectroscopy of this object, as well as Potsdam Multi Aperture Spectrograph (PMAS; Roth et al. 2005) integral-field unit (IFU) spectroscopy of its host galaxy. We show that SN 2016esw is part of the brightest tail of the SN II luminosity distribution (excluding SNe IIn or superluminous SNe II) and also exhibits some signs of interaction with CSM. Given the observed characteristics of the transient, we discuss them in comparison to other SNe II with the aim of defining its nature and constraining its physical properties.

The paper is organized as follows. Section 2 contains a description of the observations and the data. In Section 3, we describe the evolution of the light curves, colour curves, and spectra, and we estimate the reddening. We discuss our results in Section 4, and we conclude with a summary in Section 5.

2 OBSERVATIONS

2.1 Discovery

As part of the Lick Observatory Supernova Search (LOSS; Filippenko et al. 2001; Leaman et al. 2011), SN 2016esw was discovered by Halevi, Zheng & Filippenko (2016) in an unfiltered[1] image (unfiltered apparent magnitude ∼18.5) on 2016 August 8.31 (UT dates are used throughout this paper; JD = 2 457 608.81) with the 0.76 m Katzman Automatic Imaging Telescope (KAIT). The transient was located at $\alpha = 18^h58^m04^s.09 \pm 0^s.1$, $\delta = +43°56'22''.60 \pm 0''.5$ (J2000.0), and it is associated with the galaxy CGCG 229-009[2] at redshift $z = 0.02831$ (see Section 2.4). With respect to the galaxy
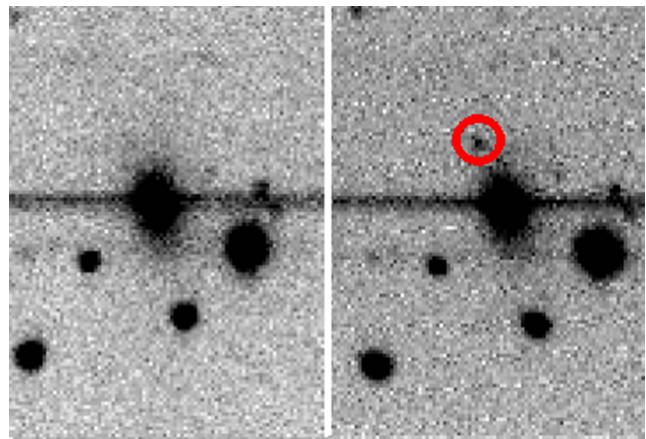
Figure 1. Left: Pre-explosion unfiltered image taken on 2016 August 7.31 with KAIT at Lick Observatory. Right: KAIT discovery unfiltered image taken on 2016 August 8.31. SN 2016esw is marked with the red circle. The horizontal streaks are artefacts produced by saturated stars.

nucleus, the object is situated $6''.85$ east and $13''.45$ north. Shivvers et al. (2016) classified the object as a SNe II owing to the presence of a blue continuum with weak, broad H Balmer lines. The most recent pre-explosion non-detection in archival images was obtained with LOSS/KAIT on 2016 August 7.31 (limiting magnitude 19.3; JD = 2 457 607.81), providing very good constraints on the explosion time (see Fig. 1).

To estimate a more accurate and precise explosion date than the mid-point (JD = 2 457 608.31 ± 0.50) between the discovery and the last non-detection epochs, the early-time unfiltered light curve (the data prior to maximum brightness and including non-detections) is fitted using a simple power law (González-Gaitán et al. 2015). We obtain an explosion date (T_{exp}) of JD = 2 457 608.33 ± 0.15 (2016 August 7.83). All observations are presented with respect to this explosion date.

2.2 Photometry

Multiband observations (*BVRI*) started only ∼2 h after the discovery, on 2016 August 8.39 with KAIT and the 1 m Nickel reflector at Lick Observatory. Automated reductions (bias and flat-field corrections and astrometric solution) had been applied to all the images using our image-reduction pipeline (Ganeshalingam et al. 2010). Even though the transient is relatively distant from its host (see Fig. 2), we took care to correctly remove the underlying host-galaxy light. The templates used for final subtractions were taken ∼450 d after the explosion and were geometrically transformed to each individual science frame.

Point spread function (PSF) photometry was performed using DAOPHOT (Stetson 1987) from the IDL Astronomy User's Library. Instrumental magnitudes were calibrated relative to a sequence of seven stars in the field of CGCG 229-009 from the AAVSO Photometric All-Sky Survey (APASS). The magnitudes were then transformed into the Landolt standard system (Landolt 1992) using the empirical prescription presented by Robert Lupton.[3] The resulting *B*, *V*, *R*, and *I* magnitudes of the local sequence stars are reported in Table 1, while the photometry for SN 2016esw is presented in Table 2. Finally, *BVRI* light curves corrected for Milky Way Galaxy

---

[1] The unfiltered band is similar to the *R* band; see Li et al. (2003).
[2] Also called 2MASX J18580350+4356090.

[3] http://classic.sdss.org/dr7/algorithms/sdssUBVRITransform.html
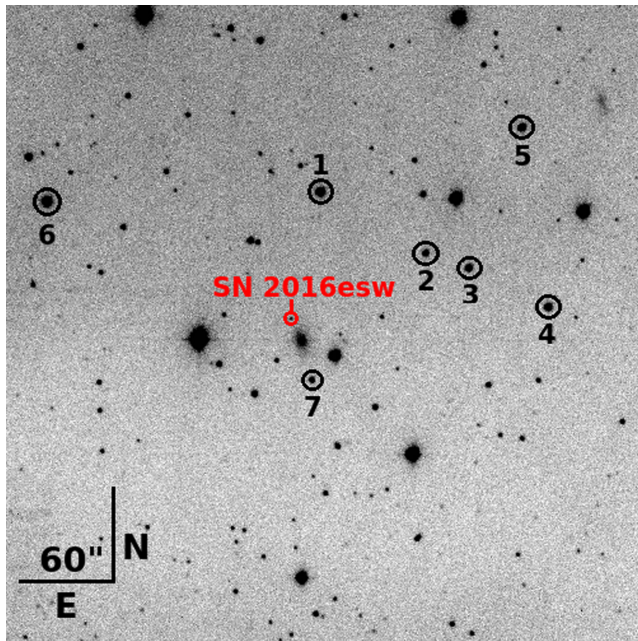
Figure 2. KAIT *I*-band image showing the location of SN 2016esw with a red circle. Reference stars are also marked with black circles.

(MWG) extinction are displayed in Fig. 3.

2.3 Optical spectroscopy

Spectroscopy of SN 2016esw began on 2016 August 8.41 ($\sim$0.6 d after explosion) using the Kitt Peak Ohio State Multi-Object Spectrograph (KOSMOS; Martini et al. 2014) mounted on the Mayall 4 m telescope at Kitt Peak National Observatory (KPNO). After this first observation, an intensive spectroscopic follow-up campaign started using the Kast double spectrograph (Miller & Stone 1993) on the Shane 3 m telescope at Lick Observatory. To minimize slit losses from atmospheric dispersion, all of the spectra were taken at the parallactic angle (Filippenko 1982). In total, we obtained nine optical spectra covering the wavelength range from $\sim$3400 to 10 500 Å with a resolution of $\sim$10 Å. Owing to visibility constraints, follow-up spectroscopy stopped on 2016 December 04.13, $\sim$118.5 d after the explosion. A detailed log of our optical observations is given in Table 3.

Spectroscopic reductions were performed using standard IRAF[4] routines. All data were debiased, flat-fielded, and cleaned of cosmic rays. Extracted 1D spectra were wavelength calibrated using Ar, He, Hg–Cs, Hg–Ar, and Ne lamps. Flux calibration was determined with instrumental sensitivity curves of spectrophotometric standard stars observed on the same night and with the same instrumental set-up. Absolute flux calibration was revised using multicolour photometry, integrating the spectral flux transmitted by standard *BVRI* filters and adjusting it by a multiplicative factor. To ensure that the resulting flux calibration is accurate to within $\sim$0.1 mag, flux calibration is performed using an iterative procedure. Atmospheric (telluric) absorption features were removed using the well-exposed spectrum of a standard star.

The spectra were corrected for MWG extinction assuming a Cardelli, Clayton & Mathis (1989) law with $R_V = 3.1$, and a dust extinction in the *V* band of 0.188 mag (Schlafly & Finkbeiner 2011). However, we do not correct for host-galaxy extinction (A_{Vh}) here, as its value is discussed in Section 3.1.5. The final spectral sequence is displayed in Fig. 4. All of the spectra are available for download from the Berkeley SuperNova DataBase (SNDB[5]; Silverman et al. 2012).

From the IFU spectroscopy of the SN 2016esw host galaxy and using the forbidden ionized nitrogen doublet [N II] ($\lambda\lambda$6583, 6548) together with the strong H α emission lines (λ6563), we measure a redshift of $z = 0.02825 \pm 0.0002$, consistent with the published redshift (0.02831; Shivvers et al. 2016). In the rest of the paper, we adopt the redshift derived from the IFU spectroscopy observation.

2.4 Host galaxy

We obtained integral field spectroscopy (IFS) of the SN 2016esw host galaxy CGCG 229-009 (3×900 s, where the second and third exposures are taken with an offset) with the PMAS (Roth et al. 2005) in PPAK (331 science fibres and 36 for sky measurements) mode (Verheijen et al. 2004) mounted on the 3.5 m telescope of the Centro Astronómico Hispano Alemán (CAHA) located at Calar Alto Observatory in Almería, Spain. The data were taken on 2017 August 18 (JD = 2 457 938), about 375 d after the explosion. At that time, the SN was almost undetectable and therefore no strong contamination is expected in the IFS analysed data. The IFS is an asset, providing additional information about both the SN position and those of the entire host galaxy. The observations are included in the PMAS/PPAK Integral-field Supernova hosts COmpilation (PISCO; Galbany et al. 2018), a sample of SN host galaxies observed with the same instrument.

The description of the data reduction is presented by Galbany et al. (2017), and our analysis follows that presented by Galbany et al. (2014, 2016b). In brief, we perform stellar population synthesis by fitting a base of simple stellar population (SSP) models to all $\sim$4000 individual spectra using STARLIGHT (Cid Fernandes et al. 2005). The best combination of SSPs is subtracted from the observed spectra to obtain a pure emission-line spectrum, and we accurately measure the flux of the most prominent continuum-free emission lines by means of weighted non-linear least-squares fits with a single Gaussian plus a linear term. From the H α emission 2D map, we select 25 H II regions by segregating clumps of emission using HIIexplorer[6] (see Sánchez et al. 2012 and Galbany et al. 2018 for criteria selection). The SN 'parent' H II region is selected as the closest to the SN 2016esw position (see Fig. 5). Note that, owing to the angular resolution of 1 arcsec (i.e. a spatial resolution of $\sim$560 pc), our selected H II regions can actually be aggregations of 1–6 classical H II regions (Mast et al. 2012). Finally, to estimate the galaxy global properties, we sum up all spectra in the 3D datacube with signal-to-noise ratio larger than 1. The resulting total spectrum is analysed following the same steps.

3 RESULTS

Here, we first describe the photometric data and analyse the light curves, the colours, and the host-galaxy extinction. Then, we discuss the spectroscopic data – including the spectral evolution, the

---

[4]IRAF is distributed by the National Optical Astronomy Observatory, which is operated by AURA, Inc., under a cooperative agreement with the U.S. National Science Foundation (NSF).

[5]http://heracles.astro.berkeley.edu/sndb/
[6]http://www.caha.es/sanchez/HII_explorer/

Table 1. *B*, *V*, *R*, and *I* local sequence star magnitudes.

Star	α (1σ) $^\circ$ ($''$)	δ (1σ) $^\circ$ ($''$)	*B* (1σ) mag (mag)	*V* (1σ) mag (mag)	*R* (1σ) mag (mag)	*I* (1σ) mag (mag)
1	284.510 (0.350)	43.962 (0.302)	14.365 (0.020)	13.715 (0.028)	13.410 (0.102)	13.032 (0.106)
2	284.484 (0.488)	43.951 (0.700)	16.045 (0.025)	15.270 (0.067)	14.860 (0.116)	14.466 (0.189)
3	284.474 (0.506)	43.948 (0.390)	15.957 (0.042)	15.000 (0.040)	14.507 (0.126)	14.013 (0.184)
4	284.455 (0.347)	43.942 (0.519)	15.958 (0.044)	14.829 (0.019)	14.210 (0.125)	13.648 (0.127)
5	284.462 (0.438)	43.973 (0.221)	15.201 (0.022)	14.487 (0.031)	14.122 (0.146)	13.728 (0.090)
6	284.576 (0.215)	43.959 (0.427)	15.099 (0.026)	13.869 (0.048)	13.241 (0.068)	12.639 (0.072)
7	284.497 (0.585)	43.924 (0.445)	16.878 (0.008)	15.952 (0.014)	15.490 (0.139)	14.998 (0.051)

Table 2. *B*, *V*, *R*, and *I* optical photometry of SN 2016esw.

JD = 2 400 000.5	Epoch days	*B* (1σ) mag (mag)	*V* (1σ) mag (mag)	*R* (1σ) mag (mag)	*I* (1σ) mag (mag)	Telescope
57608.3945	0.6	18.76 (0.11)	18.79 (0.10)	18.80 (0.08)	18.73 (0.18)	KAIT
57609.2461	1.4	18.37 (0.06)	18.45 (0.06)	18.47 (0.06)	18.32 (0.11)	KAIT
57610.1797	2.4	18.24 (0.07)	18.31 (0.08)	18.26 (0.06)	18.07 (0.12)	KAIT
57611.1797	3.4	18.08 (0.07)	18.14 (0.06)	18.06 (0.04)	18.06 (0.13)	KAIT
57612.2540	4.4	18.06 (0.06)	17.98 (0.06)	17.95 (0.06)	17.77 (0.08)	KAIT
57613.2930	5.5	18.04 (0.08)	17.93 (0.05)	17.94 (0.06)	17.68 (0.10)	KAIT
57614.2422	6.4	18.12 (0.09)	17.95 (0.06)	17.84 (0.05)	17.51 (0.10)	KAIT
57615.2422	7.4	18.04 (0.14)	17.76 (0.08)	… (…)	17.48 (0.11)	KAIT
57616.2734	8.5	18.17 (0.10)	17.89 (0.05)	17.80 (0.05)	17.55 (0.08)	KAIT
57616.3047	8.5	18.03 (0.01)	17.88 (0.01)	… (…)	17.45 (0.04)	Nickel
57617.2461	9.4	18.21 (0.10)	17.79 (0.08)	17.78 (0.06)	17.52 (0.08)	KAIT
57618.2773	10.5	18.04 (0.10)	17.93 (0.09)	17.78 (0.07)	17.48 (0.09)	KAIT
57619.3242	11.5	18.30 (0.20)	17.94 (0.14)	17.72 (0.09)	17.51 (0.15)	KAIT
57620.2891	12.5	18.19 (0.14)	18.01 (0.10)	17.79 (0.07)	17.56 (0.10)	KAIT
57621.2734	13.5	18.32 (0.11)	18.00 (0.07)	17.79 (0.05)	17.54 (0.07)	KAIT
57622.3008	14.5	18.21 (0.09)	18.03 (0.07)	17.83 (0.07)	17.64 (0.08)	KAIT
57623.2734	15.5	18.39 (0.08)	18.04 (0.06)	17.83 (0.05)	17.69 (0.08)	KAIT
57624.2656	16.5	18.42 (0.12)	17.96 (0.06)	17.83 (0.06)	17.60 (0.07)	KAIT
57625.2578	17.4	18.41 (0.08)	18.04 (0.06)	17.87 (0.04)	17.57 (0.07)	KAIT
57626.2344	18.4	18.51 (0.07)	18.01 (0.05)	17.89 (0.05)	17.60 (0.08)	KAIT
57627.2305	19.4	18.46 (0.07)	18.07 (0.04)	17.89 (0.05)	17.69 (0.07)	KAIT
57628.2305	20.4	18.48 (0.07)	18.09 (0.07)	17.85 (0.04)	17.59 (0.08)	KAIT
57629.2227	21.4	18.52 (0.08)	18.09 (0.05)	17.89 (0.04)	17.66 (0.06)	KAIT
57630.2227	22.4	18.70 (0.09)	18.15 (0.06)	17.90 (0.05)	17.71 (0.07)	KAIT
57632.2109	24.4	18.67 (0.10)	18.20 (0.06)	17.92 (0.04)	17.76 (0.07)	KAIT
57633.2188	25.4	18.72 (0.02)	18.11 (0.01)	17.85 (0.01)	17.68 (0.03)	Nickel
57633.2266	25.4	18.83 (0.11)	18.19 (0.05)	17.93 (0.05)	17.66 (0.06)	KAIT
57635.2070	27.4	18.80 (0.08)	18.22 (0.05)	17.96 (0.04)	17.66 (0.07)	KAIT
57636.2148	28.4	19.07 (0.11)	18.25 (0.05)	17.96 (0.04)	17.69 (0.06)	KAIT
57637.2109	29.4	19.01 (0.02)	18.27 (0.02)	17.92 (0.01)	17.73 (0.02)	Nickel
57638.1953	30.4	19.05 (0.11)	18.28 (0.05)	18.02 (0.05)	17.71 (0.06)	KAIT
57639.2031	31.4	19.00 (0.10)	18.33 (0.05)	18.02 (0.05)	17.77 (0.07)	KAIT
57640.2031	32.4	19.36 (0.13)	18.31 (0.06)	18.01 (0.05)	17.82 (0.07)	KAIT
57641.1875	33.4	19.19 (0.13)	18.49 (0.07)	18.02 (0.05)	17.78 (0.07)	KAIT
57642.2031	34.4	19.29 (0.18)	18.38 (0.09)	18.03 (0.06)	17.76 (0.08)	KAIT
57643.2031	35.4	19.47 (0.20)	18.30 (0.06)	18.04 (0.05)	17.71 (0.07)	KAIT
57647.2305	39.4	19.57 (0.05)	18.52 (0.03)	18.10 (0.02)	17.85 (0.03)	Nickel
57650.2227	42.4	19.75 (0.05)	18.52 (0.03)	… (…)	… (…)	Nickel
57658.1797	50.4	20.02 (0.05)	18.63 (0.02)	18.21 (0.02)	17.87 (0.03)	Nickel
57668.1836	60.4	20.31 (0.07)	18.85 (0.03)	18.31 (0.02)	18.02 (0.03)	Nickel
57683.1445	75.3	20.66 (0.10)	18.91 (0.03)	18.41 (0.02)	18.09 (0.03)	Nickel
57687.1367	79.3	20.73 (0.08)	18.98 (0.03)	18.47 (0.04)	18.13 (0.03)	Nickel
57697.1445	89.3	20.92 (0.09)	19.12 (0.03)	18.52 (0.02)	18.27 (0.04)	Nickel
57710.1133	102.3	… (…)	19.25 (0.04)	18.70 (0.03)	18.44 (0.03)	Nickel
57724.0977	116.3	… (…)	19.77 (0.06)	19.03 (0.05)	18.69 (0.05)	Nickel

expansion velocities, and the temperature. Throughout this section, the photometry and the spectra are solely corrected for MWG ex-

tinction assuming a Cardelli et al. (1989) law with $R_V = 3.1$, and a dust extinction in the *V* band of 0.188 mag (Schlafly & Finkbeiner
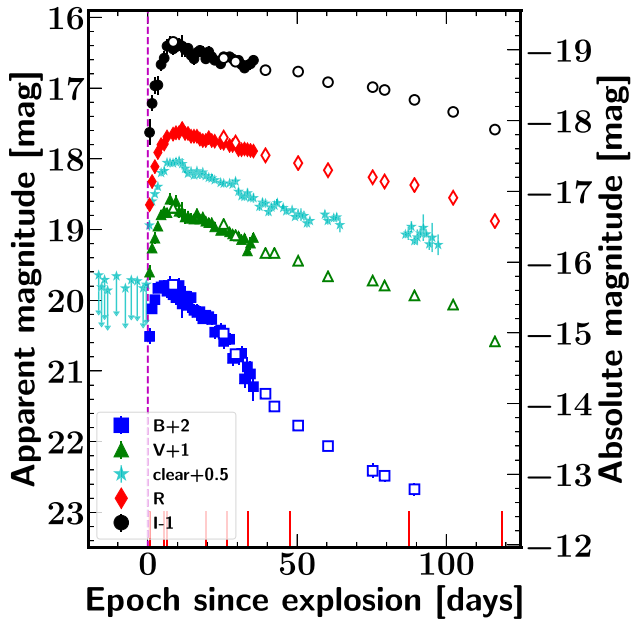
Figure 3. SN 2016esw *B*, *V*, *R*, *I*, and unfiltered light curves are shown with blue squares, green triangles, red diamonds, black dots, and cyan stars, respectively. Full and empty symbols represent the data obtained using KAIT and the Nickel telescope, respectively. Cyan arrows show the non-detections. Epochs are with respect to the explosion date (2016 August 7.81 = 0 d), which is represented by the dashed magenta vertical line. Vertical red lines represent epochs of optical spectroscopy. The apparent magnitude is shown on the left ordinate axis, while the absolute magnitude (calculated using only the distance modulus) is represented on the right. The photometry is corrected for Milky Way extinction assuming a Cardelli et al. (1989) law with $R_V = 3.1$, and a dust extinction in the *V* band of 0.188 mag (Schlafly & Finkbeiner 2011).

2011). Then, in Section 3.1.5, we discuss the value of the host-galaxy reddening (A_{Vh}) and use it in Section 4 to compare with other SNe II from the literature.

3.1 Photometry

3.1.1 Optical light curves

B, *V*, *R*, *I*, and unfiltered light curves of SN 2016esw are plotted in Fig. 3. The SN 2016esw light curves show, as is typical for SN II light curves (Anderson et al. 2014; Sanders et al. 2015; Valenti et al. 2016; Galbany et al. 2016a), a fast rise to peak magnitude, followed by a recombination phase where the hydrogen previously ionized by the SN shock recombines. The final SN II light-curve phase, called the radioactive tail (powered by the conversion of ^{56}Co into ^{56}Fe), is not seen as the object was not observable from Lick Observatory at later epochs. The start of the drop into the radioactive tail is clearly visible in the *V* band between the penultimate and the last photometric points. If the last point belonged to the plateau phase, it should have a magnitude of 19.39 [the plateau decline rate is 1.01 mag (100 d)$^{-1}$; see below]. However, the last point has a magnitude of 19.77 ± 0.06, or ∼6σ fainter than the plateau brightness at this epoch.

Note the possible presence of a double-peak structure around day 10 in the *V* band (perhaps also in the *I* and unfiltered bands), which has been previously seen in some other SNe II (e.g. SN 1999em; Leonard et al. 2002). If this structure were real, it could be attributed

to the appearance of Fe II absorption lines, which mark the onset of the recombination phase (Leonard et al. 2002). However, for SN 2016esw, we believe that the double peak is not real, as it is not seen in all of the bands; for example, we see it in the unfiltered band but not in the *R* band, yet both bands are similar (Li et al. 2003). Finally, we also believe that the feature seen in the *I* band ∼35 d after the explosion is not real, as it is not seen in the other bands.

To define the nature of the transient and to constrain its properties, here we discuss in more detail the characteristics of the *V*-band light curve, which is the band used by Anderson et al. (2014). For this purpose, following their procedure, we perform a *V*-band light-curve fitting using a linear model with four parameters: the two decline rates (s_1 and s_2), the epoch of transition between the two slopes (t_{trans}), and the magnitude offset. Then, to choose between one slope (only s_1) or two slopes (s_1 and s_2), an *F*-test is performed. Note that we only fit the optically thick phase – the epoch from maximum brightness to the end of the plateau. Fig. 6 shows the *V*-band light-curve fitting with the two slopes.

After the explosion, the *V*-band brightness rises to its maximum in ∼7 d (∼8 d in the *R* band), consistent with the average values found in the literature (Inserra et al. 2012; Gall et al. 2015; González-Gaitán et al. 2015). The maximum apparent magnitude (m_V^{max}) is 17.67 ± 0.06 mag, corresponding to an absolute magnitude $M_V^{max} = -17.79 \pm 0.06$ mag (see Section 3.1.5 for more details). The magnitude at maximum is measured by fitting a low-order polynomial to the photometry around the brightest photometric point (±5 d).

Following maximum brightness, an initial decline (s_1) lasting 60 ± 9 d at a rate of 1.83 ± 0.06 mag (100 d)$^{-1}$ is seen. After the initial cooling, the object enters the plateau phase (s_2) and the brightness declines more slowly, with a slope of 1.01 ± 0.26 mag (100 d)$^{-1}$ until 105 ± 5 d after the explosion. All these values are consistent with those derived by Anderson et al. (2014) ($s_1 = 2.65 \pm 1.50$, $s_2 = 1.27 \pm 0.93$, and OPTd = 84 ± 17); however, the optically thick phase duration (OPTd) is larger than the average value found by Anderson et al. (2014). Unfortunately, as OPTd is a combination of various SN II properties such as the hydrogen mass, radius, and interaction between ejecta and CSM, we cannot obtain direct physical constraints on the SN 2016esw progenitor from this parameter. However, it is possible from the rise, as we discuss in Section 3.1.2.

Note also that the two decline rates are lower than the average found by Anderson et al. (2014), making SN 2016esw a slow-declining SN II. It is worth noting that using the magnitude decline 50 d after maximum light proposed by Faran et al. (2014b), our object (with a decline of ∼0.9) mag is among the fast-declining SNe II.

3.1.2 Rise time

In the standard SN II light-curve evolution picture, after the first electromagnetic radiation emitted by the SN when the shock wave emerges from the stellar surface (Colgate 1974; Falk & Arnett 1977; Klein & Chevalier 1978), the early SN light curve is dominated by radiation from the expanding and cooling SN ejecta. The study of this early rise (i.e. the luminosity and the temperature evolution) can be used to constrain the progenitor radius (Waxman, Mészáros & Campana 2007; Nakar & Sari 2010; Rabinak & Waxman 2011).

First, to derive the rise times in each band, we assume that the flux is proportional to that produced by a blackbody at a fixed wavelength

Table 3. Log of optical spectroscopy of SN 2016esw.

UT Date	Epoch (days)	Tel./Instru.	Wavelength (Å)	Resolution (Å)	Exp. (s)	Observer	Reducer
2016-08-08.41	0.6	Mayall/Kosmos	4180–7060	3	1200	CK & MS	YCP
2016-08-13.28	5.5	Shane/Kast	3438–10 876	10	3600	IS	HY
2016-08-14.29	6.5	Shane/Kast	3440–10 876	10	3600	WZ	HY
2016-08-27.22	19.5	Shane/Kast	3440–10 850	10	5400	PK	HY
2016-09-03.22	26.5	Shane/Kast	3432–10 854	10	3600	BS	HY
2016-09-10.20	33.5	Shane/Kast	3426–10 878	10	3600	GH	HY
2016-09-24.16	47.5	Shane/Kast	3460–10 240	10	3600	WZ	IS
2016-11-03.16	87.5	Shane/Kast	3440–10 450	10	3660	TB,IS	TB
2016-12-04.13	118.5	Shane/Kast	3430–10 274	10	3000	TB & TdJ	TB

Note: Column 1: UT observation date. Column 2: epoch after explosion in days. Column 3: the telescope and instrument used to obtain the spectrum. Columns 4, 5, and 6: wavelength range (Å), resolution (Å), and exposure time (s), respectively. Columns 7 and 8: the observers and data reducers are indicated with their initials: CK, Charles Kilpatrick; MS, Matthew Siebert; YCP, Yen-Chen Pan; IS, Isaac Shivvers; HY, Heechan Yuk; WZ, WeiKang Zheng; PK, Patrick Kelly; GH, Goni Halevi; BS, Benjamin Stahl; TB, Thomas Brink; TdJ, Thomas de Jaeger.
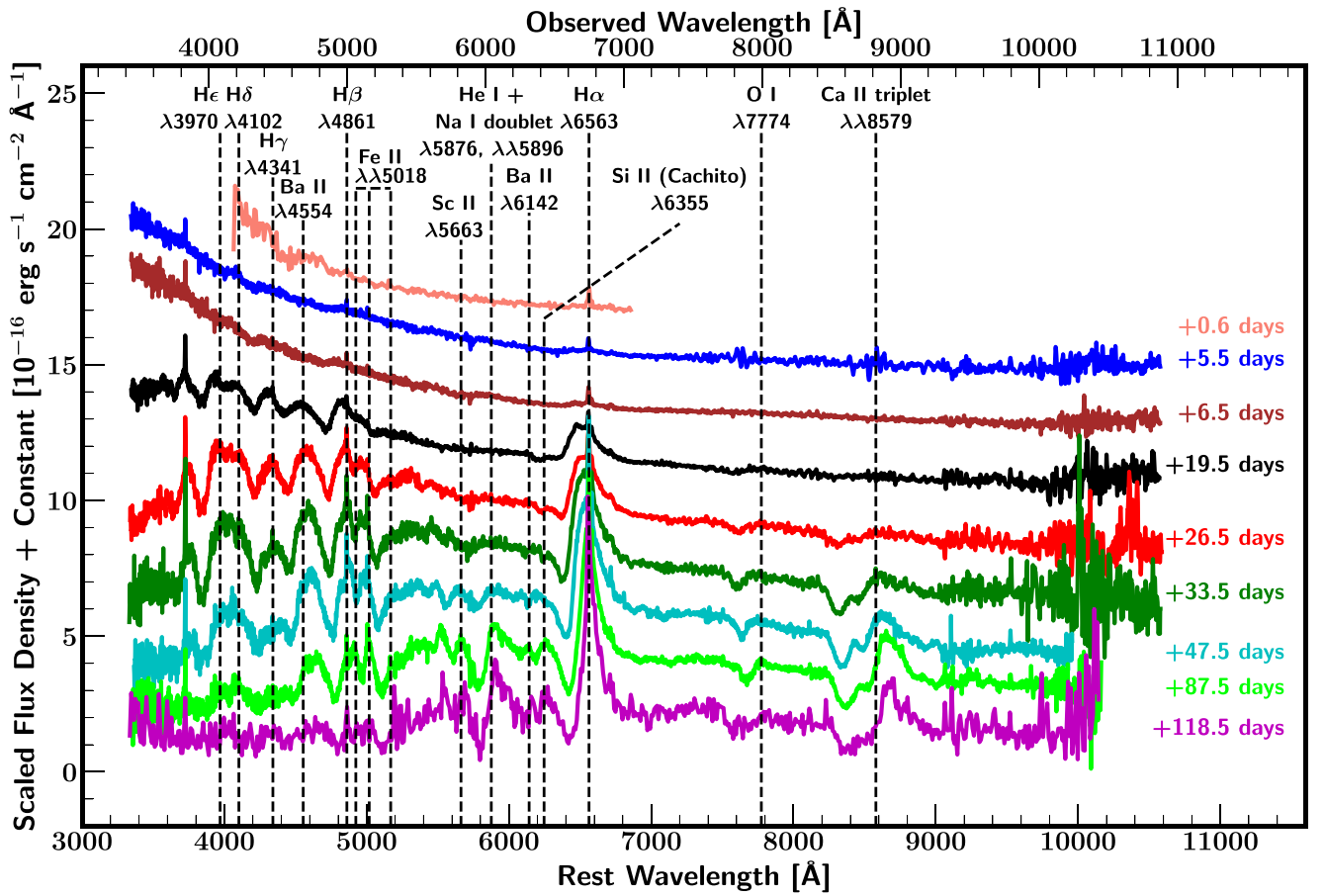
Figure 4. Optical spectra of SN 2016esw taken with the KPNO/Mayall and Lick/Shane telescopes. On the right, the epochs are listed with respect to the explosion (2016 August 7.81 = 0 d). Telluric absorption features were removed. The flux calibration of the spectra was revised using multicolour photometry. The spectra have been corrected for MWG extinction but not for host-galaxy reddening.

(Waxman, Mészáros & Campana 2007; Cowen, Franckowiak & Kowalski 2010). We fit the early-time light curves using the model defined by Cowen et al. (2010) and also used by Roy et al. (2011) and Yuan et al. (2016):

$$f(t) = \frac{A}{e^{B(t-t_0)^\alpha} - 1}(t - t_0)^\beta , \qquad (1)$$

where t_0 is the time of explosion, and α, β, A, and B are free parameters. Note that α and β depend on the temperature evolution and the expansion of the photospheric radius, respectively. The fits for the four bands (B, V, R, and I) are shown in Fig. 7. Finally, the rise time is taken as the period between the explosion date (JD = 2 457 608.33 ± 0.15) and the epoch of maximum flux obtained from the derivative of equation (1). We derive rise-time values of 6.4, 9.6, 11.3, and 10.8 d for B, V, R, and I, respectively. These
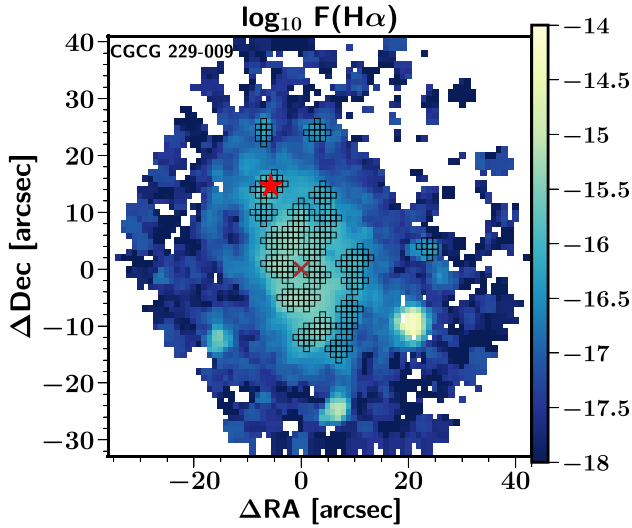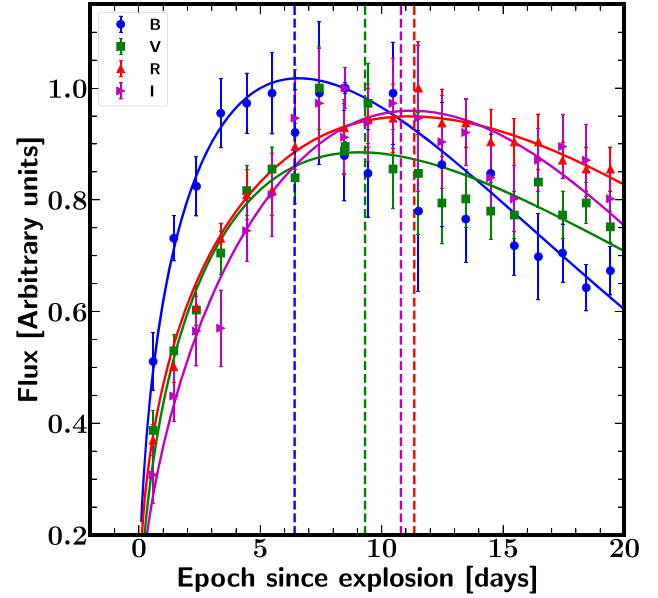
Figure 5. Continuum-subtracted H α emission map of CGCG 229-009. The transparent black squares represent the HII regions extracted with HII explorer. The red star and brown cross represent (respectively) the location of SN 2016esw and the CGCG 229-009 nucleus. The three bumps (white) in the southern part of the galaxy are field stars and, therefore, not selected in our HII region analysis.
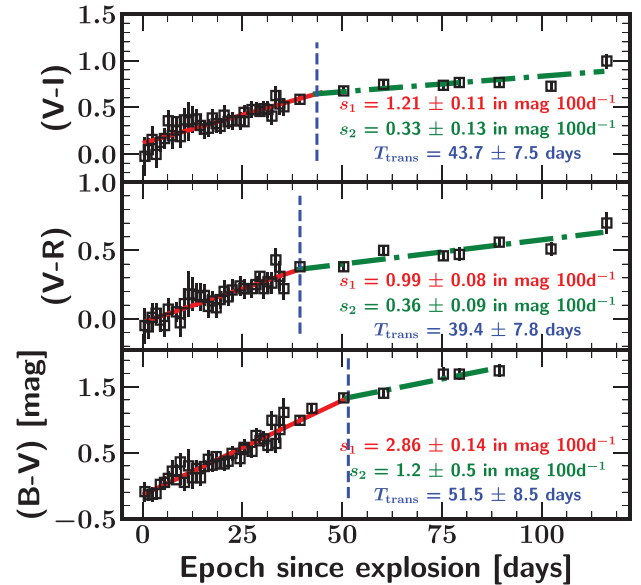

Figure 7. The flux normalized to the maximum brightness of each filter (*B*, *V*, *R*, and *I*) is shown with blue dots, green squares, red up triangles, and magenta right triangles, respectively. Solid lines are the fits to equation (1) and vertical dotted lines mark the end of the rise.

Figure 6. *V*-band light-curve fitting following the Anderson et al. (2014) procedure. Cyan line is obtained using only one slope while the lines in black and red is using two slopes. The photometry is only corrected for Milky Way extinction.

Figure 8. Observed $(B - V)$, $(V - R)$, and $(V - I)$ colour evolution of SN 2016esw corrected for Milky Way extinction. In each panel, we fit the colour curves using two slopes; the first is represented by a red line while the second by a dashed-dot green line.

3.1.3 Pre-explosion radius

To first order, the rise-time duration depends only on the progenitor radius, as the effects of the mass and energy are negligible (Nakar & Sari 2010; Rabinak & Waxman 2011; Gall et al. 2015; González-Gaitán et al. 2015). For this reason, using Nakar & Sari (2010) analytical models, here we perform only a simple parameter study to estimate the progenitor radius. For this, we create a grid of models by varying the progenitor radius (50–700 R$_\odot$ in steps of 10 R$_\odot$)

values are consistent with those derived by studies using large SN II samples, such as González-Gaitán et al. (2015) or Gall et al. (2015). Note that these rise times are faster than the analytical and hydrodynamical rises obtained from standard RSG models (Gall et al. 2015; González-Gaitán et al. 2015).
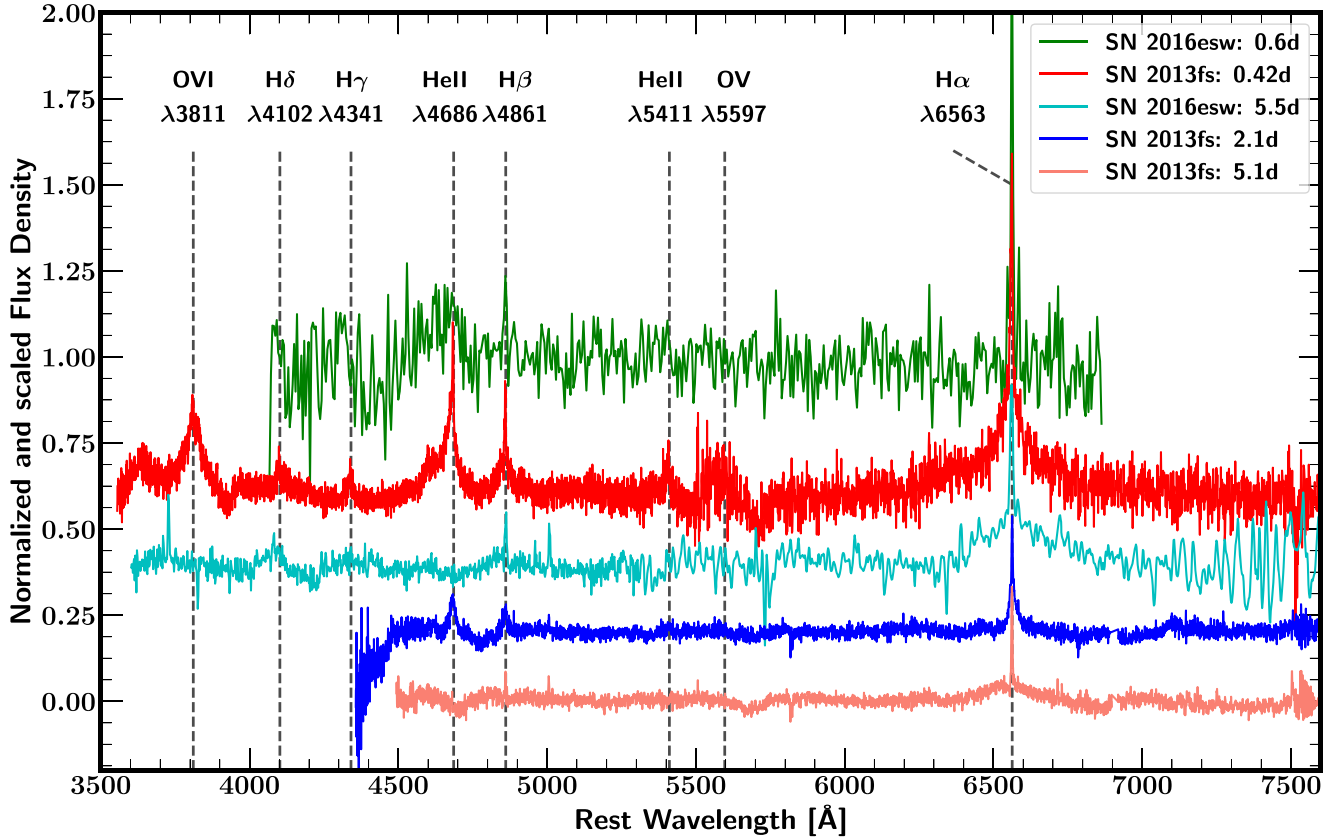
Figure 9. Early-time spectroscopy of SN 2013fs (Yaron et al. 2017) and SN 2016esw. All of the spectra have been normalized and scaled for clarity.

with a fixed explosion energy of 1.0×10^{51} erg and a fixed stellar mass of $15\,M_\odot$. These stellar mass and energy values are typical of core-collapse SNe (see Smartt et al. 2009 for a review, and references therein).

For all these models, we derive a blackbody spectral energy distribution (SED) using the temperature defined by Nakar & Sari (2010) in their equation (31) and normalized by the bolometric luminosity defined in equation (29). Finally, for each band, we compare the rise times from the different models (taken as the maximum) and those derived in the previous subsection. We obtain an average radius of $190 \pm 50\,R_\odot$ ($R \approx 220, 230, 200$, and $100\,R_\odot$ for B, V, R, and I, respectively). Again, these values are consistent with those found in the literature. From the observed rise times, González-Gaitán et al. (2015) and Gall et al. (2015) derived RSG radii of 200–500 $R_\odot$ – that is, smaller than the typical radius used in analytical or hydrodynamical RSG models ($>500\,R_\odot$). Note also that this method of extracting a rise time from the analytical models and comparing it to the observed rise time has been recently questioned by Rubin et al. (2016), as the models are valid only for a brief period (4 d). Finally, the fast rise observed in SN II light curves could be explained by the presence of CSM rather than small RSG radii (Morozova, Piro & Valenti 2017a).

3.1.4 Colours

The $(B - V)$, $(V - R)$, and $(V - I)$ colour curves of SN 2016esw are presented in Fig. 8. All the colours show the same generic behaviour expected for SNe II (de Jaeger et al. 2018a): they consist of two linear regimes which are correlated. During the first ∼40–50 d, the

object quickly becomes redder as the SN envelope expands and cools. After this first phase, the SN colour changes more slowly as the rate of cooling decreases.

Initially, the $(B - V)$ colour increases with a rate of 2.86 ± 0.14 mag (100 d)$^{-1}$, followed by a slower increase of only 1.20 ± 0.50 mag (100 d)$^{-1}$. The transition between the two phases occurs 51.5 ± 8.5 d after the explosion. These values differ from those of de Jaeger et al. 2018, except the first slope. Indeed, with a sample of ∼60 SNe II, we derive average values for the two slopes of $s_{1,(B - V)} = 2.63 \pm 0.62$ mag (100 d)$^{-1}$ and $s_{2,(B - V)} = 0.77 \pm 0.26$ mag (100 d)$^{-1}$, and a transition time $T_{\mathrm{trans},(B - V)} = 37.7 \pm 4.3$ d.

Regarding $(V - R)$, the slopes are less steep, because the SED is less sensitive to temperature changes in the red than in the blue part of the SED. The $(V - R)$ colour curve is characterized by an initial slope of 0.99 ± 0.08 mag (100 d)$^{-1}$, followed by a second slope of 0.36 ± 0.09 mag (100 d)$^{-1}$. The transition between the two regimes occurs 39.4 ± 7.8 d after the explosion.

Finally, via the same procedure, we find that the $(V - I)$ colour becomes redder with an initial slope of 1.21 ± 0.11 mag (100 d)$^{-1}$, followed by a slope of 0.33 ± 0.13 mag (100 d)$^{-1}$ and a transition at 43.7 ± 7.5 d. A detailed comparison with other SN II colours is given in Section 4.1.

3.1.5 Extinction and absolute magnitude

To derive intrinsic properties of the SN explosion, it is important to correct the photometry for dust reddening from the MWG and also from the host galaxy.
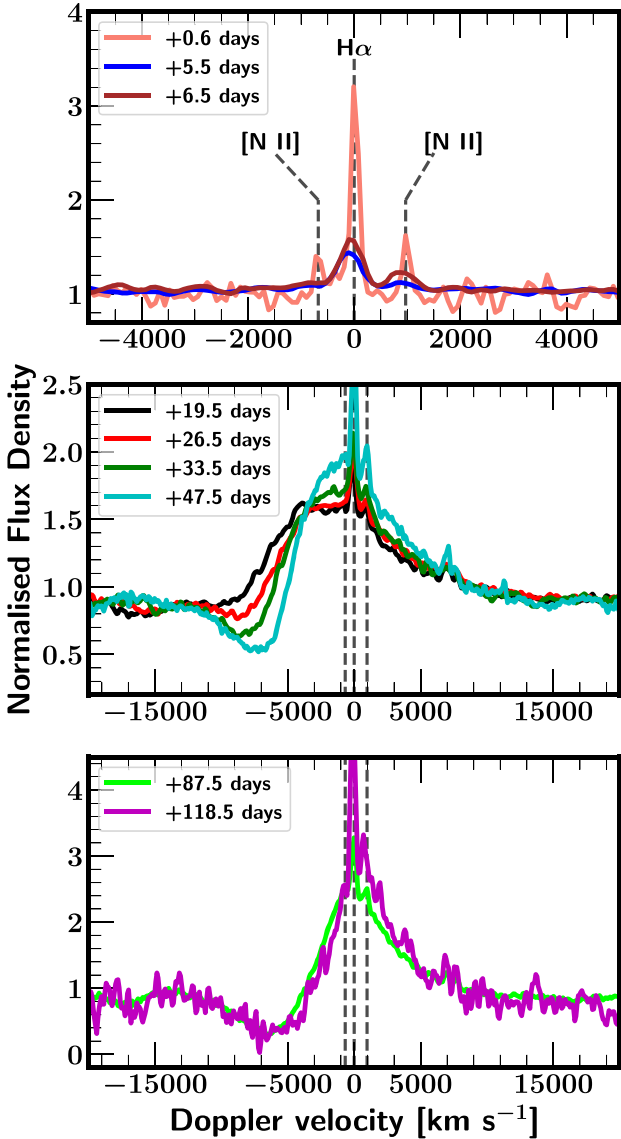
Figure 10. Close-up views centred on H α. The spectra are separated in three phases: early-time (top), plateau (middle), and plateau end (bottom). In all the panels, the vertical dashed lines correspond to [NII] λλ6548, 6583 and H α. Narrow (spectrally unresolved) emission lines are almost certainly produced by a contaminating HII region.

The Galactic extinction is straightforward using the dust map of Schlafly & Finkbeiner (2011). For SN 2016esw, the MWG extinction in the *V* band is 0.188 mag.[7] Then, assuming a host-galaxy $z = 0.02825$ and a ΛCDM cosmology ($\Omega_\Lambda = 0.70$, $\Omega_M = 0.30$), with $H_0 = 70 \, \text{km s}^{-1} \, \text{Mpc}^{-1}$, we obtain a distance of 123.6 Mpc. This distance implies an absolute magnitude at maximum corrected only for Galactic extinction of $M_V = -17.79 \pm 0.06$ mag.

To estimate the host-galaxy extinction, different methods are used in the literature, such as the Na I D equivalent width (Turatto, Benetti & Cappellaro 2003; Poznanski et al. 2011) or the colour excess at the end of the plateau (Hamuy 2003; Olivares et al. 2010). However, the validity of the Na I D method with low-resolution spectra (as
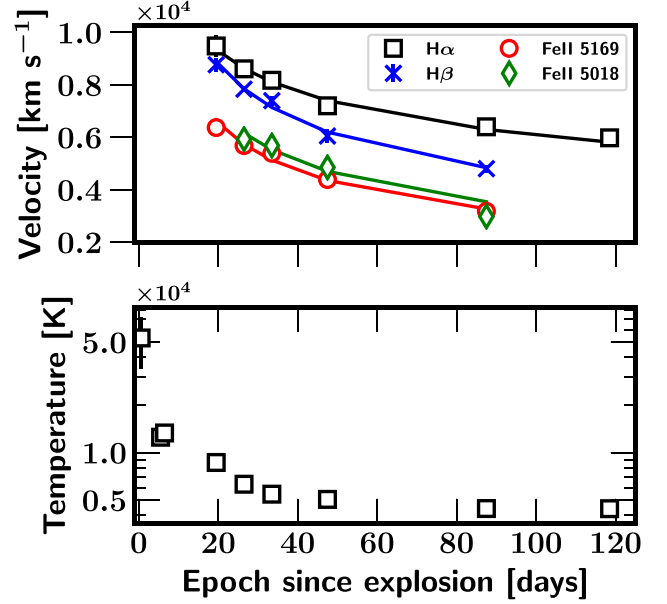
Figure 11. *Top:* Expansion velocities of H α, H β, FeII λ5018, and Fe II λ5169. *Bottom:* Blackbody temperature evolution.

in our case) has been questioned (Poznanski et al. 2011; Phillips et al. 2013; Galbany et al. 2017). The colour method has also been debated, as to use the method the authors assume the same intrinsic colour for all SNe II, which seems to not be true (Faran et al. 2014a, de Jaeger et al. 2018).

Despite this warning, and to compare with other studies in the literature which use one of these methods, we try to estimate the host-galaxy reddening using both methods. First, with the Na I D equivalent width (EW) method and using the relation found by Turatto et al. (2003) ($E(B - V) \approx 0.16$ EW Na I D − 0.01), we obtain $E_{\text{host}}(B - V) = 0.185 \pm 0.031$ mag (EW Na I D = 1.08 ± 0.13 Å). Secondly, as our data do not show the transition between the plateau and the radiative tail, we cannot use the method proposed by Olivares et al. (2010). Nor can we use the method derived by Hamuy (2003), which consists of comparing the ($B - V$) colour at the end of the plateau with the prototypical SN II SN 1999em for which a precise host-galaxy extinction is well known ($E_{\text{host}}(B - V) = 0.07$ mag; Leonard et al. 2002). Indeed, our *B*-band photometry stops before reaching the end of the plateau (∼110 d).

In the rest of this paper, we assume a host-galaxy extinction of $E_{\text{host}}(B - V) = 0.185 \pm 0.031$ mag. Using this value, an absolute magnitude at maximum of $M_V = -18.36 \pm 0.11$ mag is derived, where the error includes the uncertainties in the magnitude and host-galaxy extinction measurements. For completeness, as it is discussed in Section 4.3, we have also direct host-galaxy estimates from the IFU data, and both values are in perfect agreement ($E_{\text{host}}(B - V) \approx 0.18$ mag from the IFU).

3.2 Spectroscopy

In this part, we describe the spectral evolution of our object, together with its velocity evolution. A full comparison with objects from the literature will be given in Section 4.
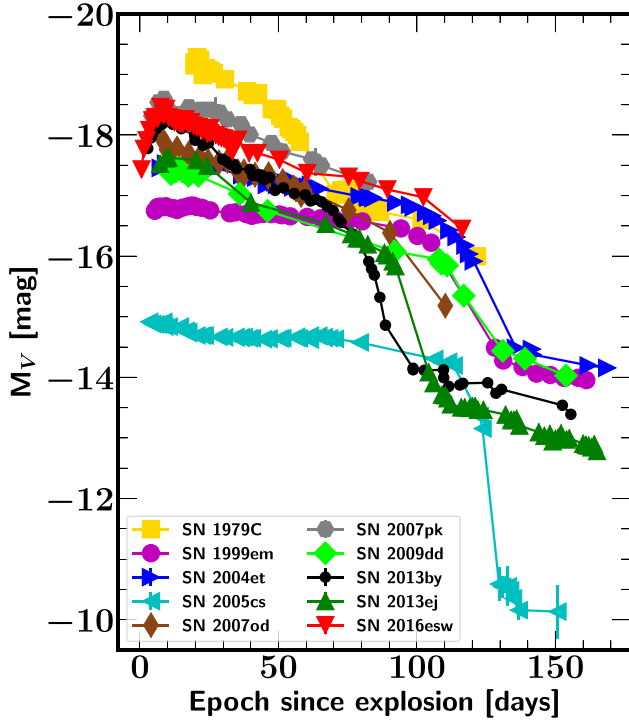
Figure 12. Comparison of the *V*-band light curve of SN 2016esw with those of other well-observed SNe II: SN 1999em (Leonard et al. 2002), SN 2004et (Maguire et al. 2010), SN 2005cs Pastorello et al. (2009), SN 2007od (Inserra et al. 2011), SN 2007pk (Inserra et al. 2013), SN 2009dd (Inserra et al. 2013), SN 2013by (Valenti et al. 2015), and SN 2013ej (Huang et al. 2015). The fast-declining SN 1979C de Vaucouleurs et al. (1981) is also shown.

3.2.1 Spectral evolution

Fig. 4 shows the optical-wavelength spectral evolution of SN 2016esw from 0.6 to 118.5 d after explosion. The first spectrum reveals a blue featureless continuum consistent with a young core-collapse SN. The next two spectra also show a nearly featureless blue continuum, as well as a few narrow emission lines from the host galaxy (see Section 3.2.2). As the photosphere cools down, the broad Balmer lines grow stronger, and at day +19.5, the H α feature shows a boxy shape with a flat absorption profile suggesting possible ejecta–CSM interaction (Inserra et al. 2011). At day +26.5, the evidence of interaction starts to cease, and then the object follows a typical SN II evolution. The Fe II lines start to appear in the blue part of the spectra (e.g. Fe II λ5018, Fe II λ5169), as well as the Ca II near-IR triplet ($\lambda\lambda$8498, 8542, 8662) and the O I λ7774 absorption line. Present until days +88, these lines get stronger with time. Around days +33.5 and +47.5, close to the previous He I λ5876 line, a new feature arises and evolves with time to a strong P-Cygni profile. This line is the sodium doublet Na I D $\lambda\lambda$5889, 5095. At day +47.5 we start to see, in addition of all the previously mentioned lines, the Sc II λ5663 and Ba II λ6142 lines. Unfortunately, the last spectrum, at day +118.5, is too noisy to see lines other than the prominent Balmer and Ca II near-IR triplet features. It is also important to note that between epochs +19.5 and +33.5 d after the explosion, the H α P-Cygni profile shows an atypical shape produced by 'Cachito', which is an extra absorption component on the blue side of H α associated with Si II at early epochs (Gutiérrez et al. 2017). When it disappears the P-Cygni profile becomes normal.
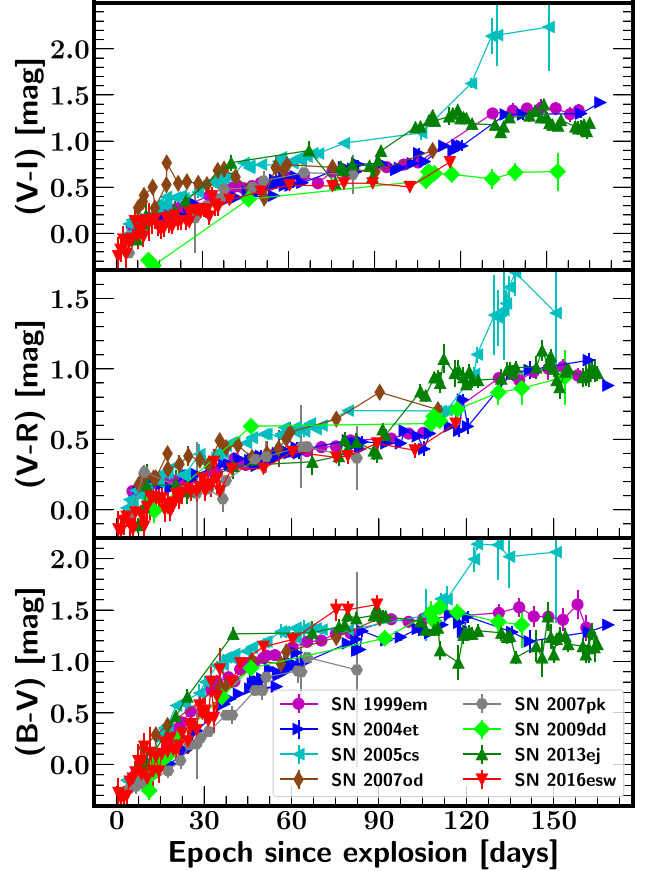
Figure 13. Comparison of the $(B - V)$, $(V - R)$, and $(V - I)$ colour curves of SN 2016esw with those of other well-observed SNe II: SN 1999em (Leonard et al. 2002), SN 2004et (Maguire et al. 2010), SN 2005cs Pastorello et al. (2009), SN 2007od (Inserra et al. 2011), SN 2007pk (Inserra et al. 2013), SN 2009dd (Inserra et al. 2013), and SN 2013ej (Huang et al. 2015).

### 3.2.2 Early-time spectroscopy

Recent studies (Gal-Yam et al. 2014; Groh 2014; Shivvers et al. 2015; Khazov et al. 2016; Yaron et al. 2017) have shown that early-time spectra (1–2 d after the explosion) can be dominated by strong, high-ionization emission lines produced by the recombination of dense CSM ionized by first the shock-breakout flash (Gal-Yam et al. 2014) and second by ultraviolet light emitted during the week after the RSG explosion (Dessart et al. 2017). Early-time spectral observations are challenging and still uncommon in the literature; thus, here we present a comparison with SN 2013fs (iPTF13dqy; Yaron et al. 2017).

In Fig. 9, we compare our two earliest spectra (0.6 d and 5.5 d[8]) of SN 2016esw with those of SN 2013fs at epoch of 0.42 d (10.1 h), 2.1 d, and 5.1 d. Unlike SN 2013fs, our first spectrum does not exhibit strong, narrow emission lines of He II λ4686, He II λ5411, or O V λ5597. The absence of high-ionization oxygen lines is expected, as they should disappear within ~11 h after the explosion (Yaron et al. 2017). However, the He II emission lines from a strong progenitor wind should be visible until ~5 d after the explosion (Khazov et al. 2016). Our two spectra taken at 5.5 d and 6.5 d do not reveal

---

[8]For clarity, we omit the spectrum taken 6.5 d after the explosion; it is nearly identical to the one taken at 5.5 d.

Table 4. Observed blackbody temperatures and expansion velocities of SN 2016esw.

UT date	Epoch (days)	T_{bb} (K)	$v(H\alpha)$ (km s^{-1})	$v(H\beta)$ (km s^{-1})	$v(Fe\,II\,\lambda5018)$ (km s^{-1})	$v(Fe\,II\,\lambda5169)$ (km s^{-1})
2016-08-08.41	0.6	53 150 (19 100)	… (…)	… (…)	… (…)	… (…)
2016-08-13.28	5.5	12 500 (1100)	… (…)	… (…)	… (…)	… (…)
2016-08-14.29	6.5	13 330 (1200)	… (…)	… (…)	… (…)	… (…)
2016-08-27.22	19.5	8650 (500)	9480 (410)	8770 (250)	… (…)	6375 (270)
2016-09-03.22	26.5	6300 (350)	8615 (100)	7840 (100)	5930 (120)	5690 (150)
2016-09-10.20	33.5	5450 (300)	8175 (80)	7400 (180)	5690 (110)	5390 (170)
2016-09-24.16	47.5	5050 (300)	7200 (130)	6050 (250)	4850 (100)	4390 (180)
2016-11-03.16	87.5	4420 (250)	6400 (180)	4800 (150)	2980 (200)	3175 (130)
2016-12-04.13	118.5	4410 (300)	5985 (300)	… (…)	… (…)	… (…)
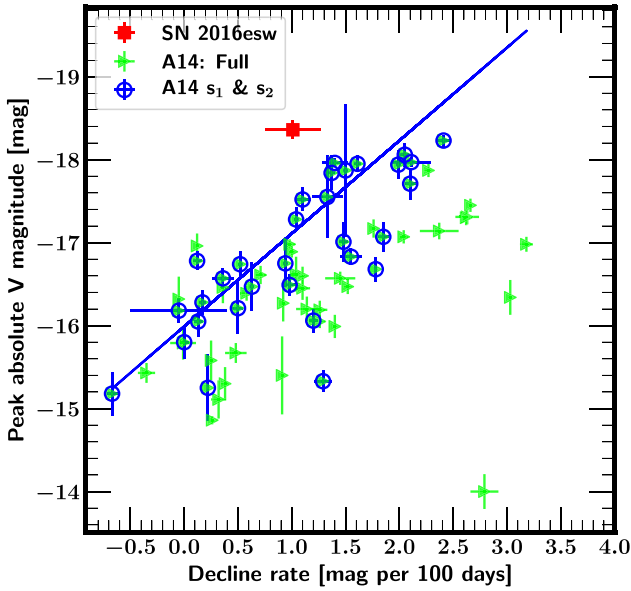
Figure 14. Correlation between M_{max} and s_2. Green right triangles represent the full sample used by Anderson et al. (2014) while the red square is SN 2016esw. The blue line shows the linear relation ($M_{max} = -1.12\,s_2 - 15.99$) between M_{max} and s_2 derived by Anderson et al. (2014) using only SNe with s_1 and s_2 (blue circles).

Table 5. Properties of our sample of Type II supernovae.

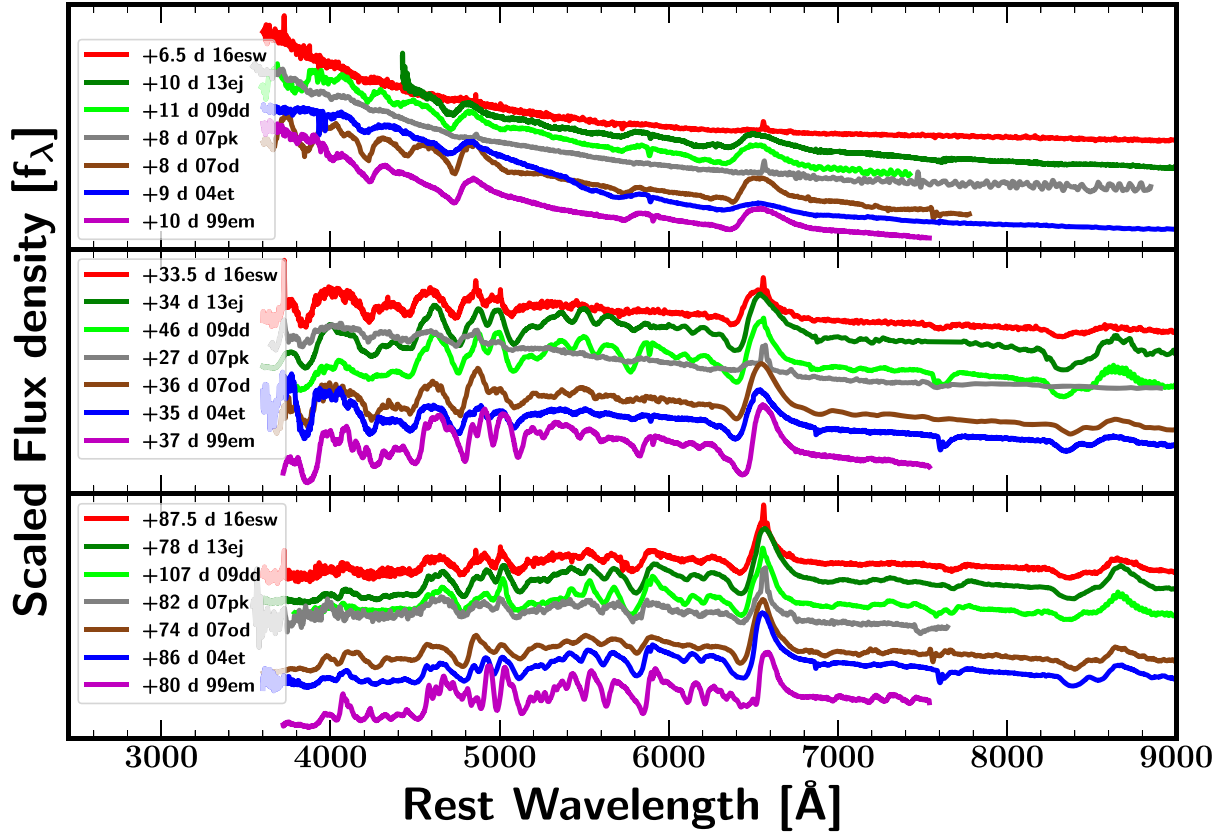| SN	Explosion Epoch (MJD)	D (Mpc)	$E(B-V)_{tot}$ (MWG + host; mag)	Refs
1979C	2 443 967	15.2	0.023 + 0.130	1, 2, 3
1999em	2 451 476	11.7	0.030 + 0.070	4
2004et	2 453 270	5.9	0.300 + 0.110	5
2005cs	2 453 549	7.1	0.030 + 0.020	6
2007od	2 454 404	24.9	0.038 + 0.000	7
2007pk	2 454 412	70.1	0.050 + 0.060	8
2009dd	2 454 925	14.1	0.020 + 0.430	8
2013by	2 456 404	14.8	0.195 + 0.000	9
2013ej	2 456 497	9.6	0.061 + 0.000	10
2016esw	2 457 608	123.6	0.061 + 0.185	11

References: (1) Weiler et al. (1986), (2) Freedman et al. (2001), (3) de Vaucouleurs et al. (1981), (4) Leonard et al. (2002), (5) Maguire et al. (2010), (6) Pastorello et al. (2009), (7) Inserra et al. (2011), (8) Inserra et al. (2013), (9) Valenti et al. (2015), (10) Bose et al. (2015), (11) This work.

up view centred on H α. The spectra show characteristic lines of an H II region (e.g. [N II] $\lambda\lambda6548$, 6583); thus, we believe that the spectrally unresolved H α line superposed on the broader H α profile is produced mainly or entirely by host-galaxy contamination. Note also that this line is present in all of our spectra, even those without clear signs of interaction, supporting a host-galaxy origin rather than CSM interaction.

3.2.3 Expansion velocity and temperature

We investigate the expansion velocities of H α $\lambda6563$, together with lines used for the standard candle method (Hamuy & Pinto 2002; Nugent et al. 2006; D'Andrea et al. 2010; Poznanski, Nugent & Filippenko 2010; de Jaeger et al. 2017a,b) – H β $\lambda4861$, Fe IIλ 5018, and Fe II $\lambda5169$. All of the velocities are measured through the minimum flux of the absorption component of the P-Cygni line profile after correcting the spectra for the heliocentric redshift of the host galaxies. Uncertainties in the velocities were obtained by measuring many times the minimum of the absorption (changing the continuum fit each time) and determining their standard deviation. We are not able to measure the velocities in the first three spectra, as the Balmer lines are strongly contaminated by the host-galaxy emission lines and no clear absorption is seen. All of the velocities are reported in Table 4 and plotted in Fig. 11.

SN II velocity evolution is well known and decreases following a power law (Hamuy 2001): with time, the photosphere advances deeper into the ejecta, and thus we see material moving at progressively lower velocities. The SN 2016esw velocity evolution

He II emission lines, but rather a blue continuum with weak H α emission. These two spectra are very similar to those of SN 2013fs at 5.1 d after explosion. At this epoch, the He II emission lines seen at earlier epochs in spectra of SN 2013fs disappear completely; instead, there is an almost featureless blue continuum (with only weak Balmer lines).

In SN 2016esw, the absence of high-ionization emission lines at early phases could suggest a lack of dense CSM around the progenitor; alternatively, perhaps it was not observed at sufficiently early epochs (Khazov et al. 2016; Dessart et al. 2017). As our first observed spectrum was taken only 0.6 d after the explosion, the most plausible explanation is the absence of dense material near the star's surface. Given that we detect signs of interaction at later epoch (19.5 d after the explosion; see Section 3.2.1), we believe that the progenitor was surrounded by low-density CSM, but not near the star's surface and not ejected during the final stage ($\sim$1 yr) prior to explosion, in contrast to the case of SN 2013fs.

Finally, all three of our early-time spectra exhibit very narrow H α (and H β) emission lines which could be caused by a contaminating H II region or by CSM interaction. In Fig. 10, we illustrate a close-

Figure 15. Comparison of early-time (10 d), plateau (35 d), and end of the plateau (80 d) spectra of SN 2016esw with those of other well-studied Type II SNe: SN 1999em (Baron et al. 2000), SN 2004et (Sahu et al. 2006; Maguire et al. 2010; Guillochon et al. 2016), SN 2007od (Inserra et al. 2011; Hicken et al. 2017), SN 2007pk (Inserra et al. 2013; Hicken et al. 2017), SN 2009dd (Inserra et al. 2013), and SN 2013j (Huang et al. 2015; Dhungana et al. 2016). All comparison spectra are corrected for extinction and redshift (adopted values in Table 5).

follows this behaviour and is characterized by power-law exponents of -0.264 ± 0.011, -0.405 ± 0.014, -0.459 ± 0.020, and -0.465 ± 0.018 for H α $\lambda6563$, H β $\lambda4861$, Fe II $\lambda5018$, and Fe II $\lambda5169$, respectively (fits are shown in Fig. 11). These values are very consistent with those found in the literature. de Jaeger et al. (2017b), using the whole Carnegie Supernova Project I sample, derived for the H β velocity an exponent of -0.407 ± 0.173. On the other hand, using the Fe II $\lambda5169$ line, Nugent et al. (2006) and de Jaeger et al. (2015) derived values of -0.464 ± 0.017 and -0.55 ± 0.20, respectively. Finally, as expected, since the H α and H β lines are formed above the photosphere (i.e. at larger radii), their velocities are higher than those derived for the Fe II lines which are better connected to the photospheric velocity.

For all the spectra, we perform a blackbody fit and derive the temperature, as shown in Table 4 and in Fig. 11. The temperature evolution is rather normal for a SN II, with a broken power law described by a rapid decline at early phases followed by a slower decline at later epochs (Faran, Nakar & Poznanski 2017). Indeed, the early spectra taken only 5.5–6.5 d after the explosion show a blue continuum with a hot blackbody temperature of $T_{bb} \approx 12,500$ K. Subsequently the temperature drops about 5000 K in only $\sim$30 d. Finally, after this first decline ($\sim$30 d after the explosion), the hydrogen envelope starts to recombine and the temperature evolves more slowly, with a decrease of only $\sim$1000 K in $\sim$50 d.

4 DISCUSSION

Here, we compare our object properties with those of a sample of other well-observed SNe II, including the well-studied prototypical SN II SN 1999em ($M_V \approx -16.94$ mag; Hamuy et al. 2001; Leonard et al. 2002; Elmhamdi et al. 2003). The sample also contains the prototype of fast-declining SNe II (historically SNe IIL), SN 1979C ($M_V \approx -19.45$ mag; Branch et al. 1981; de Vaucouleurs et al. 1981), together with well-observed SNe II similar to SN 2016esw in optically thick duration (SN 2004et; $M_V \approx -17.5$ mag; Sahu et al. 2006; Maguire et al. 2010) or brightness: SN 2007od ($M_V \approx -18.0$ mag; Inserra et al. 2011), SN 2013by ($M_V \approx -18.2$ mag; Valenti et al. 2015), and SN 2013ej ($M_V \approx -17.8$ mag; Valenti et al. 2014; Bose et al. 2015; Huang et al. 2015; Mauerhan et al. 2016; Dhungana et al. 2016). We also select two SNe II from the moderately luminous SN II sample of Inserra et al. (2013), as both objects show ejecta–CSM interaction: SN 2007pk ($M_V \approx -18.44$ mag) and SN 2009dd ($M_V \approx -17.46$ mag). A subluminous SN II is also added: SN 2005cs ($M_R \approx -15.2$ mag; Pastorello et al. 2009). The explosion epochs (second column), distances[9] (third column), and extinctions (fourth column) for each SN are detailed in Table 5.

[9]Hubble constant of 70 km s^{-1} Mpc^{-1} and a ΛCDM Universe with $\Omega_M = 0.3$ and $\Omega_\Lambda = 0.7$.
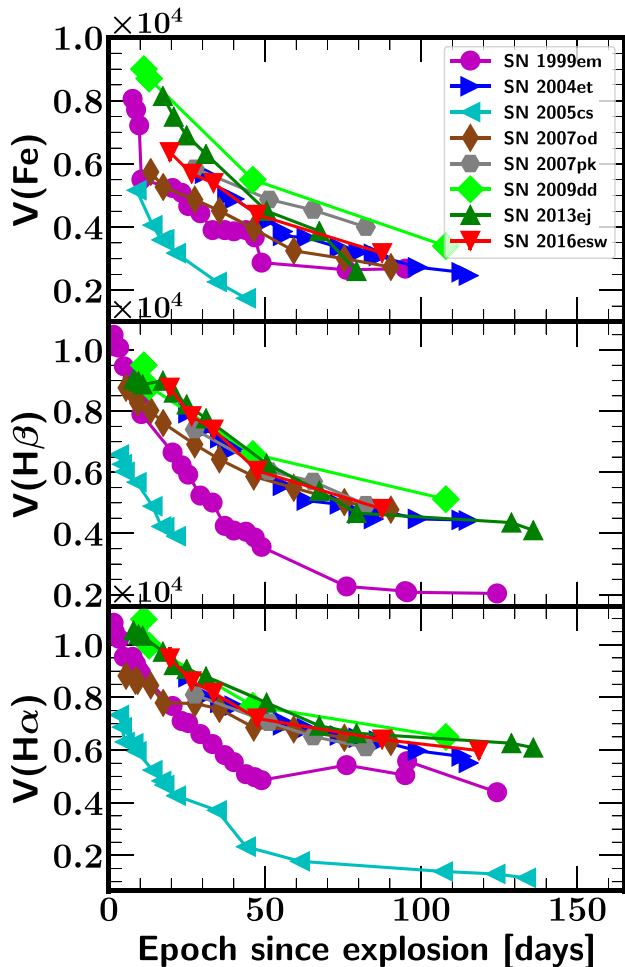
Figure 16. Evolution of the H α (bottom), H β (middle), and Fe II λ5169 (top) velocities of SN 2016ew compared with those of SN 1999em (Leonard et al. 2002), SN 2004et (Maguire et al. 2010), SN 2005cs Pastorello et al. (2006, 2009), SN 2007od (Inserra et al. 2011), SN 2007pk (Inserra et al. 2013), SN 2009dd (Inserra et al. 2013), and SN 2013ej (Huang et al. 2015). All velocities are expressed in units of 10^4 km s^{-1}.

4.1 Photometry

Fig. 12 shows a comparison of the *V*-band light curves of SN 2016esw and other well-observed SNe II. We clearly see that SN 2016esw is much more luminous than the prototypical SN II (SN 1999em); it is in the bright tail end of the SN II luminosity distribution. For example, with a peak absolute magnitude of −18.32, our object is more luminous than SN 2013by ($M_V \approx -18.2$ mag) or SN 2007od ($M_V \approx -18.0$ mag). However, SN 2016esw is fainter than SN 2007pk ($M_V \approx -18.44$ mag) and SN 1979C ($M_V \approx -19.45$ mag). SN 2007pk shows strong ejecta–CSM interaction and was first classified as a SN IIn (Parisky & Li 2007). On the other hand, SN 1979C has a *V*-band light curve with a very steep decline during the photospheric phase.

Regarding the *V*-band light-curve behaviour, SN 2016esw has a longer recombination phase than the majority of luminous SNe II (SN 2007od, SN 2009dd, SN 2013by, and SN 2013ej). However, the *V*-band light curve is comparable to that of SN 2004et, with the same recombination-phase duration (∼110 d) but with a brighter plateau (by ∼0.2 mag). Though the late-time light curves of SN 2016esw and SN 2004et are similar, at early times they show differences

possibly caused by CSM interaction. For SN 2016esw, the initial decline after maximum brightness is much steeper than for SN 2004et. The *V* light curve of SN 2016esw also displays similarities to that of SN 2007pk regarding the brightness, but after 40 d SN 2007pk is more linear than our object.

In Fig. 13, we show a comparison of the (*B−V*), (*V−R*), and (*V−I*) colour curves with those of the well-observed SNe II used in the previous paragraph. The (*B−V*) trend of SN 2016esw is very similar to that of normal SNe II (e.g. SN 1999em), and the (*V−R*) and (*V−I*) colour curves do not show a red peak after ∼100 d as seen for SN 2005cs. Finally, the colours also confirm the similarities to SN 2004et and SN 2007pk, with nearly identical (*V−R*) and (*V−I*) colour evolution. However, at late epochs SN 2016esw seems to have a redder (*B−V*) colour than do SN 2004et or SN 2007pk.

It is also important to note that even if the *V*-band light curve belongs to the SN II family, SN 2016esw seems to not follow the correlation found by Anderson et al. (2014) between the absolute peak magnitude and the slope of the plateau ($M_V = -1.12\,s_2 - 15.99$ mag). Even if SN 2016esw is not considered an outlier according to the Chauvenet (1863) criterion, it exhibits a flatter slope than the other luminous SNe II – that is, for its absolute peak magnitude ($M_V = -18.36$ mag), SN 2016esw should have a slope of ∼2.10 mag (100 d)$^{-1}$ instead of 1.01 ± 0.26 mag (100 d)$^{-1}$. This could be important for cosmology with SNe II: to reduce the Hubble-diagram scatter, one of the methods used to standardize SNe II is based on the absolute magnitude versus s_2 correlation (photometric colour method; de Jaeger et al. 2015). Fig. 14 shows the peak magnitude versus s_2 correlation from Anderson et al. (2014) and where our object lies

4.2 Spectroscopy

Fig. 15 displays a spectroscopic comparison between SN 2016esw and our well-studied SN II sample defined in Table 5 at three different epochs: early phase (∼10 d), plateau phase (∼35 d), and the end of the recombination phase (∼80 d).

Qualitatively, the comparison shows that the SN 2016esw spectra are broadly similar to others after 30 d past explosion. In particular, after this epoch, SN 2016esw and SN 2004et become mostly indistinguishable in terms of observable line features and their evolution. Both of these SNe II also exhibit identical absorption-component strengths, indicating similar temperatures. However, the spectra of SN 2016esw have shallower H α absorption, which is attributed to differences in progenitor properties; for example, fast-declining SNe II have smaller absorption (Gutiérrez et al. 2014).

At early epochs, SN 2016esw (along with SN 2007pk) is quite different from the other SNe II, with a featureless blue continuum and resolved narrow Balmer emission lines. As SN 2007pk is known to have relatively strong ejecta-CSM interaction (Inserra et al. 2013), we believe that the SN 2016esw early-time spectra are also contaminated by some interaction between the ejecta and CSM; evidence for CSM is also visible in the spectrum taken 19.5 d after the explosion (see Section 3.2.1). The fact that these two SNe II are also among the most luminous SNe II advocates in favour of CSM interaction at early epochs, as some luminosity could be added from the CSM interaction. Additionally, the plateau length could be supported by such interaction. Even if the effect on the plateau length is very small with respect to the impact on the early-time light curve, Morozova et al. (2017b) demonstrated that hydrodynamical models with a dense wind fit the data better than those without the dense wind (models with CSM have a longer plateau).
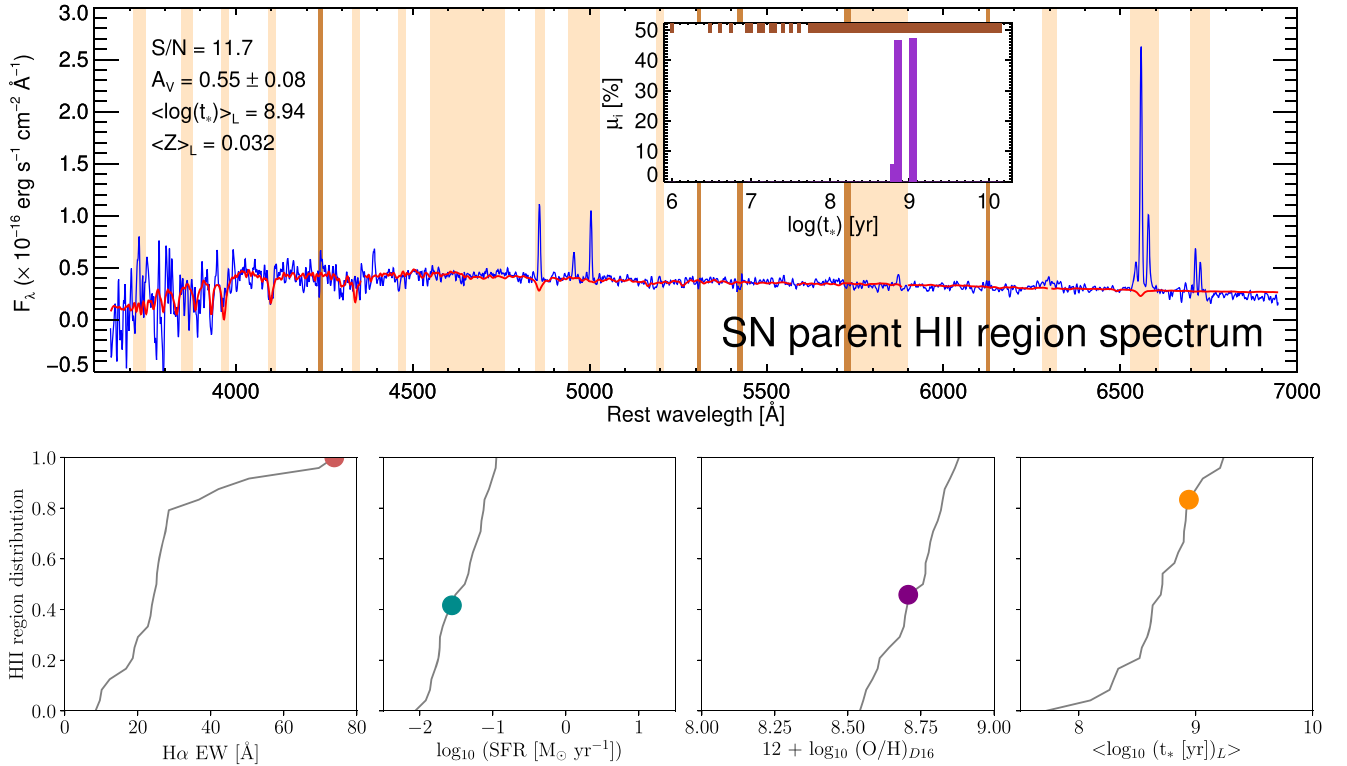
Figure 17. *Top:* SN 2016esw parent H II region spectrum and best simple stellar population fit from STARLIGHT (red). Vertical strips represent masked regions in the fit due to known emission lines (such as Balmer lines, oxygen, WR bumps, etc.; in beige) and regions with night-sky lines (in brown). The inner panel shows the SFH of the spectrum (in purple), where the upper brown tick marks represent the ages of the models used in the fit. The signal-to-noise ratio of the spectrum, optical extinction, average stellar age, and average metallicity are reported in the upper-left corners. *Bottom:* Distributions of H α equivalent width, star-formation rate, oxygen abundance, and average stellar age of all 25 H II regions in CGCG 229-009. Dotted colours represents the position of the SN 2016esw parent H II region in these distributions.

Finally, at late epochs, both objects also display very similar spectra, with nearly identical absorption-component strengths (e.g. H α). However, at epoch ~+ 30 d after the explosion, the two spectra differ. This difference might be explained by the fact that their spectra represent snapshots of the transition from interacting SNe II to normal SNe II, but the phases are not quite the same and the transitions may have proceeded at different rates.

In Fig. 16, we compare the H α, H β, and FeII $\lambda5169$ velocity evolution of SN 2016esw with those of our comparison sample (SN 1999em, SN 2004et, SN 2005cs, SN 2007od, SN 2007pk, SN 2009dd, and SN 2013ej). For the three lines, SN 2016esw velocities are comparable to those of the majority of our sample but higher than the prototypical Type II SN 1999em and much higher than SN 2005cs, a low-luminosity SN II which is known to have slow photospheric expansion. It is important to note again the similarity with SN 2004et and SN 2007pk, where the velocities are almost identical to those of our object.

4.3 Stellar populations at the SN location

SN II progenitors are massive stars ($M_{ZAMS} \geq 8\,M_\odot$; see Smartt et al. 2009) that exploded a few tens of Myr after they were born predominantly within the dense cores of giant molecular clouds (surrounded by H II regions). From the 2D H α emission-line map, we detected 25 H II regions and assigned the closest in distance to SN 2016esw as the 'parent' H II region, with the assumption that

its progenitor was born there and shares the region's properties. We present the spectrum of the SN parent H II region in the top panel of Fig. 17, while in the bottom panel we show normalized cumulative distributions of four parameters: H α equivalent width (proxy for age; Kuncarayakti et al. 2013; Galbany et al. 2014); the star formation rate (SFR), which is proportional to the H α luminosity (Kennicutt 1998); the oxygen abundance as a proxy for the metal content (in the Dopita et al. 2016 D16 calibrator); and the luminosity-weighted average stellar age. These four parameters are measured in the spectra of the 25 H II regions found in CGCG 229-09. In each panel, we highlight where the SN parent H II region is located in these distributions.

As seen in the top panel of Fig. 17 where the star formation history (SFH) is displayed, STARLIGHT only needs three models of ages around 1 Gyr (600, 700, and 1100 Myr) to get the best fit to the spectrum. However, the presence of emission lines suggests ongoing star formation happening in the region. In fact, we show that this H II region has the highest H α EW of all HII regions in the galaxy (73.82 $\pm$ 2.64 Å). This, combined with its low-to-average SFR ($\log_{10}[SFR/(M_\odot\,yr^{-1})] = -1.56 \pm 0.06$ dex) compared to all H II regions in the galaxy, can be explained by a projection effect where a small amount of gas (given the low/average SFR) is being ionized by young stars in the foreground, on top of an older stellar continuum in the background. This is reinforced by the fact that even having a low/average SFR, this HII region has an older luminosity-weighted average age ($\log_{10}(t/yr) = 8.94 \pm 0.14$
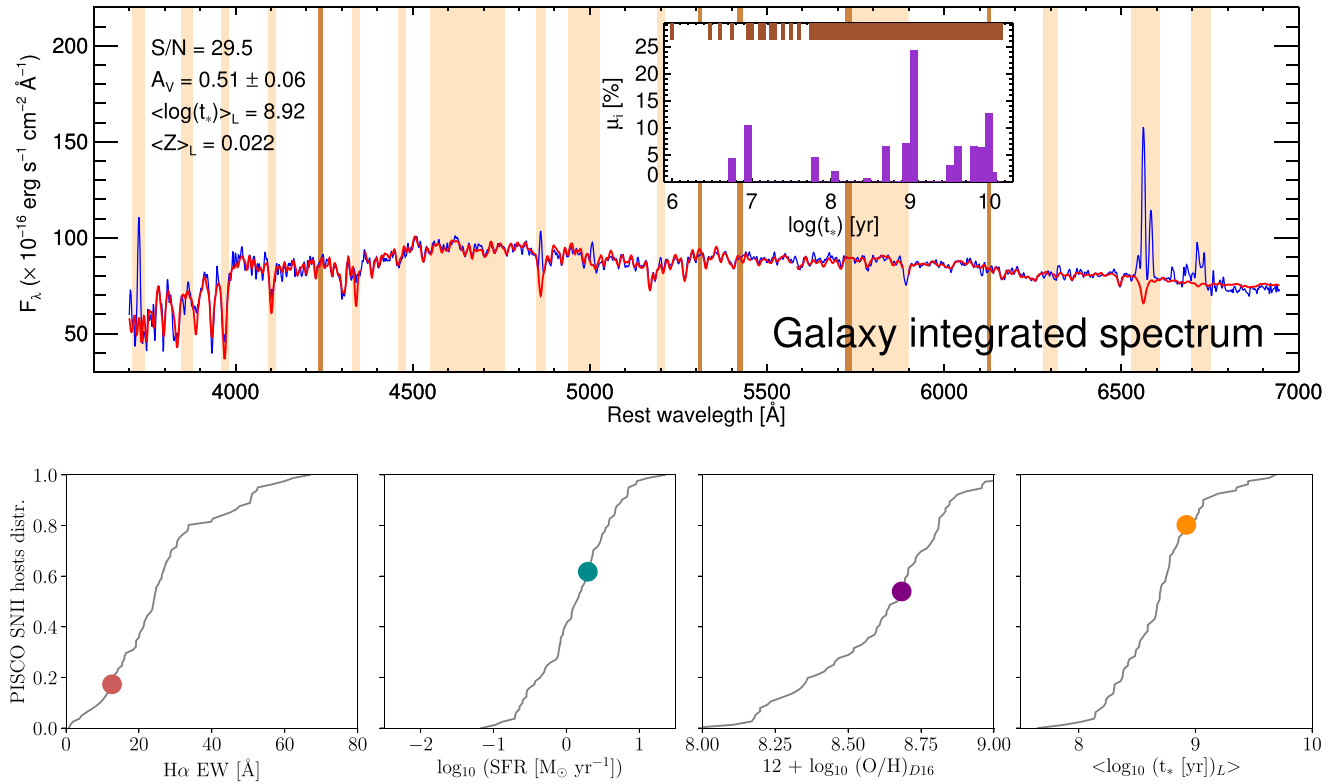
Figure 18. *Top:* CCG 229-009 integrated spectrum and best simple stellar population fit from STARLIGHT (red). Vertical strips represent masked regions in the fit due to known emission lines (such as Balmer lines, oxygen, WR bumps, etc.; in beige) and regions with night-sky lines (in brown). The inner panel shows the SFH of the spectrum (in purple), where upper brown tick marks represent the ages of the models used in the fit. The signal-to-noise ratio of the spectrum, optical extinction, average stellar age, and average metallicity are reported in the upper left corners. *Bottom row:* Distributions of the same parameters of all 82 SN II host galaxies in PISCO (Galbany et al. 2018). Dotted colours represents the position of CGCG 229-009 in these distributions.

dex) than their counterparts (see lower right panel in Fig. 17).

The optical extinction in the local SN 2016esw environment can be estimated through the Balmer decrement (Stasińska et al. 2004) in the continuum-subtracted spectrum. Assuming Case B recombination (typical of heating sources with $T \approx 10^4$ K and large optical depths; Osterbrock & Ferland 2006), we find $A_{Vh} = 0.55 \pm 0.08$ mag (i.e. $E(B - V) \approx 0.18$ mag). Although this is totally independent of our previous estimate using the Na I D EW (see Section 3.1.5), all of the values are very consistent. This confirms the host-galaxy extinction adopted in this work, $E(B - V) \approx 0.185$ mag.

The luminosity-weighted stellar metallicity is above solar ($Z_\odot = 0.02$) with a value $<Z>_L = 0.03$ (i.e. $1.5 Z_\odot$), and it is in agreement with the estimated oxygen abundance, $12 + \log_{10}(O/H) = 8.71$ dex. However, note that the luminosity-weighted stellar metallicity tells us the chemical composition when the stars were formed, not the current one of the gas. Since most of the population was formed at very early times (see Fig. 17), which is compatible with our current understanding of the SFH in galaxies, then the stellar metallicity should be lower than the current gas-phase one (unless there is a huge amount of accretion). With respect to the other H II regions in the host galaxy, the SN parent H II region has an average oxygen abundance value.

A metallicity estimate can also be directly obtained using the SN spectra, as the strengths of metal lines are strongly dependent on progenitor metallicity (Dessart et al. 2014). In Fig. 19, we compare

four theoretical models (Dessart et al. 2014) with distinct progenitor metallicities (0.1, 0.4, 1, and 2 times $Z_\odot$) at 50 d after the explosion together with the SN 2016esw spectrum at 47.5 d after the explosion. We clearly see that the strengths of metal lines in the blue part of the SN 2016esw spectrum are a better fit to the high-metallicity models (1–$2 Z_\odot$) than to those of low metallicity (0.1–$0.4 Z_\odot$). This is consistent with the value derived from the SN parent H II region, where a metallicity of $1.5 Z_\odot$ is found.

One could suggest a possible relation between the peak luminosity and the metallicity; however, Anderson et al. (2016) did not find such a correlation. On the other hand, Taddia et al. (2016) found that SN II peak magnitudes correlate with Z, but in the sense that brighter SNe II may occur at lower Z, which is opposite what we found with our object (luminous SN II and high-metallicity progenitor). Note also from this figure that the SN 2016esw spectrum corrected for MWG and host-galaxy extinctions fits perfectly the unextinguished theoretical models, again supporting the host-galaxy extinction value we derived.

Additionally, we present the integrated spectrum of CGCG 229-009 in Fig. 18 and the best SSP fit from STARLIGHT. The lower panels show normalized cumulative distributions of the same four parameters presented in Fig. 17 measured in integrated spectra of all 82 SN II host galaxies from PISCO. The coloured dots represent the position of CGCG 229-009 within these distributions.

From the SFH shown in Fig. 18 (top panel), we see that STARLIGHT needs a wide variety of SSPs of different ages (between 10 Myr and 10 Gyr), although the luminosity-weighted average age

(8.92 ± 1.23 dex) is quite similar to the SN 2016esw parent H II region (8.94 ± 0.14 dex). From the lower panel of Fig. 18, we see that CGCG 229-009 is in the 20th percentile of old SN hosts in the PISCO sample, consistent with being in the 20th percentile of the galaxies with lower average H α EW (12.63 ± 1.40 Å) as both quantities correlate.

Finally, both the SFR (0.29 ± 0.43 dex) and the oxygen abundance (8.68 dex) are very close to the average values for all PISCO SN II hosts, although the SFR is a bit higher than the mean. The main differences between our local and global environment analyses come from the H α EW, which is relatively high when looking at the SN position, but low when studying the global properties.

5 CONCLUSIONS

In this paper, for the first time, we show photometric and spectroscopic data on SN 2016esw, together with a study of its host galaxy. Thanks to our rapid follow-up observations from less than 1 d after the explosion up to 120 d later, and to a comparison with other SNe II from the literature, we find a number of interesting similarities with the family of luminous SNe II, as well as some peculiar properties that help us understand the great SN II variety in the Universe. Our detailed observations should provide useful comparisons with models of SNe II. We summarize the properties of SN 2016esw as follows.

(i) SN 2016esw is a luminous SNe II, with an absolute magnitude (M_V) at maximum brightness between −17.79 and −18.36 mag (depending on the assumed host-galaxy extinction). As for other unusually luminous SNe II (SN 2007pk or SN 2013by), there might be a contribution from CSM–ejecta interaction.

(ii) Ejecta–CSM interaction is also suggested by the early-time spectra (<6.5 d) showing a nearly featureless blue continuum with few narrow emission lines, and by the boxy H α profile at epoch 19.5 d. The mostly identical spectroscopic evolution with SN 2007pk, known to be characterized by strong ejecta–CSM interaction, also favours such an interpretation.

(iii) The early-time spectra (0.6 d, 5.5 d, and 6.5 d) do not exhibit strong high-ionization emission lines as seen in SNe II having progenitors closely surrounded by dense CSM (e.g. SN 2013fs).

(iv) During the transition between an interacting to a normal SN II (19.5–33.5 d), SN 2016esw spectra exhibit an H α P-Cygni profile with an atypical shape produced by an extra absorption component on the blue side associated with Si II.

(v) SN 2016esw also has an unusually long, flat, plateau slope relative to its luminosity; it seems to not follow the well-known relation between the luminosity and the plateau decline rate (Anderson et al. 2014).

(vi) From the early-time light curves, the derived rise times are consistent with those from studies of large SN II samples, and comparisons with analytical models lead to a small progenitor radius (∼200 R$_\odot$).

(vii) Using host-galaxy information, a high-metallicity progenitor ($Z \approx 1.5 Z_\odot$) is derived. SN 2016esw does not follow the correlation found by Taddia et al. (2016) that more luminous SNe II occur at lower Z.

REFERENCES

Anderson J. P. et al., 2014, ApJ, 786, 67
Anderson J. P. et al., 2016, A&A, 589, A110
Barbon R., Ciatti F., Rosino L., 1979, A&A, 72, 287
Baron E. et al., 2000, ApJ, 545, 444
Bose S. et al., 2015, ApJ, 806, 160
Branch D., Falk S. W., Uomoto A. K., Wills B. J., McCall M. L., Rybski P., 1981, ApJ, 244, 780
Cardelli J. A., Clayton G. C., Mathis J. S., 1989, ApJ, 345, 245
Chauvenet W., 1863, A Manual of Spherical and Practical Astronomy, Vol. II. J. B. Lippincott & Company, Philadelphia, PA
Chevalier R. A., 1976, ApJ, 207, 872
Chevalier R. A., 1981, ApJ, 251, 259
Cid Fernandes R., Mateus A., Sodré L., Stasińska G., Gomes J. M., 2005, MNRAS, 358, 363
Colgate S. A., 1974, ApJ, 187, 333

Cowen D. F., Franckowiak A., Kowalski M., 2010, Astropart. Phys., 33, 19
de Jaeger T. et al., 2015, ApJ, 815, 121
de Jaeger T. et al., 2017a, MNRAS, 472, 4233
de Jaeger T. et al., 2017b, ApJ, 835, 166
de Jaeger T. et al., 2018, MNRAS, , 476, 4592
Dessart L. et al., 2014, MNRAS, 440, 1856
Dessart L. et al., 2017, A&A, 605, 83
de Vaucouleurs G., de Vaucouleurs A., Buta R., Ables H. D., Hewitt A. V., 1981, PASP, 93, 36
Dhungana G. et al., 2016, ApJ, 822, 6
Dopita M. A., Kewley L. J., Sutherland R. S., Nicholls D. C., 2016, Ap&SS, 361, 61
D'Andrea C. B. et al., 2010, ApJ, 708, 661
Elias-Rosa N. et al., 2010, ApJ, 714, L254
Elias-Rosa N. et al., 2011, ApJ, 742, 6
Elmhamdi A. et al., 2003, MNRAS, 338, 939
Falk S. W., Arnett W. D., 1977, ApJS, 33, 515
Faran T., Nakar E., Poznanski D., 2018, MNRAS, 473, 513
Faran T. et al., 2014a, MNRAS, 442, 844
Faran T. et al., 2014b, MNRAS, 445, 554
Filippenko A. V., 1982, PASP, 94, 715
Filippenko A. V., 1988, AJ, 96, 1941
Filippenko A. V., 1991, in Danziger I. J., Kjaer K., eds, European Southern Observatory Conference and Workshop Proceedings, Vol. 37, p. 343
Filippenko A. V., 1997, ARA&A, 35, 309
Filippenko A. V., Li W. D., Treffers R. R., Modjaz M., 2001, in Paczynski B., Chen W.-P., Lemme C., eds, ASP Conf. Ser. Vol. 246, IAU Colloq. 183: Small Telescope Astronomy on Global Scales, Astron. Soc. Pac., San Francisco, p. 121
Filippenko A. V., Matheson T., Ho L. C., 1993, ApJ, 415, L103
Fransson C., 1982, A&A, 111, 140
Freedman W. L. et al., 2001, ApJ, 553, 47
Gal-Yam A. et al., 2014, Nature, 509, 471
Galbany L. et al., 2014, A&A, 572, A38
Galbany L. et al., 2016a, AJ, 151, 33
Galbany L. et al., 2016b, A&A, 591, A48
Galbany L. et al., 2017, MNRAS, 468, 628
Galbany L. et al., 2018, ApJ, 855, 107
Gall E. E. E. et al., 2015, A&A, 582, A3
Ganeshalingam M. et al., 2010, ApJS, 190, 418
González-Gaitán S. et al., 2015, MNRAS, 451, 2212
Grassberg E. K., Imshennik V. S., Nadyozhin D. K., 1971, Ap&SS, 10, 28
Groh J. H., 2014, A&A, 572, L11
Guillochon J., Parrent J., Kelley L. Z., Margutti R., 2016, ApJ, 835, 64
Gutiérrez C. P. et al., 2014, ApJ, 786, L15
Gutiérrez C. P. et al., 2017, ApJ, 850, 90
Halevi G., Zheng W., Filippenko A. V., 2016, Transient Name Server Discovery Report, 542
Hamuy M., 2003, ApJ, 582, 905
Hamuy M., Pinto P. A., 2002, ApJ, 566, L63
Hamuy M. A., 2001, PhD thesis, The University of Arizona
Hamuy M. et al., 2001, ApJ, 558, 615
Hicken M. et al., 2017, , ApJS, 263, 6
Huang F. et al., 2015, ApJ, 807, 59
Inserra C. et al., 2011, MNRAS, 417, 261
Inserra C. et al., 2012, MNRAS, 422, 1122
Inserra C. et al., 2013, A&A, 555, A142
Kennicutt R. C., Jr, 1998, ARA&A, 36, 189
Khazov D. et al., 2016, ApJ, 818, 3
Klein R. I., Chevalier R. A., 1978, ApJ, 223, L109
Kuncarayakti H. et al., 2013, AJ, 146, 31
Landolt A. U., 1992, AJ, 104, 340
Leaman J., Li W., Chornock R., Filippenko A. V., 2011, MNRAS, 412, 1419

Leonard D. C. et al., 2002, PASP, 114, 35
Li W., Filippenko A. V., Chornock R., Jha S., 2003, PASP, 115, 844
Maguire K. et al., 2010, MNRAS, 404, 981
Martini P. et al., 2014, in Ground-based and Airborne Instrumentation for Astronomy V. p. 91470Z (arXiv:1407.4541)
Mast D. et al., 2014, A&A, 561, 129
Mauerhan J. C. et al., 2016, ApJ, 834, 118
Miller R. P. S., Stone R. P., 1993, Lick Observatory Technical Report No. 66, University of California, Santa Cruz
Morozova V., Piro A. L., Valenti S., 2017b, ApJ, 838, 28
Morozova V., Piro A. L., Valenti S., 2018, ApJ, 858, 15
Nakar E., Sari R., 2010, ApJ, 725, 904
Nugent P. et al., 2006, ApJ, 645, 841
Olivares E. F. et al., 2010, ApJ, 715, 833
Osterbrock D. E., Ferland G. J., 2006, Astrophysics of Gaseous Nebulae and Active Galactic Nuclei. University Science Books, Sausalito, CA
Parisky X., Li W., 2007, Cen. Bur. Electron. Telegr., 1129
Pastorello A. et al., 2006, MNRAS, 370, 1752
Pastorello A. et al., 2009, MNRAS, 394, 2266
Phillips M. M. et al., 2013, ApJ, 779, 38
Popov D. V., 1993, ApJ, 414, 712
Poznanski D., Ganeshalingam M., Silverman J. M., Filippenko A. V., 2011, MNRAS, 415, L81
Poznanski D., Nugent P. E., Filippenko A. V., 2010, ApJ, 721, 956
Rabinak I., Waxman E., 2011, ApJ, 728, 63
Roth M. M. et al., 2005, PASP, 117, 620
Roy R. et al., 2011, ApJ, 736, 76
Rubin A. et al., 2016, ApJ, 820, 33
Sahu D. K., Anupama G. C., Srividya S., Muneer S., 2006, MNRAS, 372, 1315
Sanders N. E. et al., 2015, ApJ, 799, 208
Schlafly E. F., Finkbeiner D. P., 2011, ApJ, 737, 103
Schlegel E. M., 1990, MNRAS, 244, 269
Shivvers I., Groh J. H., Mauerhan J. C., Fox O. D., Leonard D. C., Filippenko A. V., 2015, ApJ, 806, 213
Shivvers I., Zheng W., Yuk H., Filippenko A. V., 2016, Astron. Telegr., 9381
Silverman J. M. et al., 2012, MNRAS, 425, 1789
Smartt S. J., 2009, ARA&A, 47, 63
Smartt S. J., Eldridge J. J., Crockett R. M., Maund J. R., 2009, MNRAS, 395, 1409
Stasińska G., Mateus A., Jr, Sodré L., Jr, Szczerba R., 2004, A&A, 420, 475
Stetson P. B., 1987, PASP, 99, 191
Sánchez S. F. et al., 2012, A&A, 546, A2
Taddia F. et al., 2016, A&A, 587, L7
Turatto M., Benetti S., Cappellaro E., 2003, in Hillebrandt W., Leibundgut B., eds, From Twilight to Highlight: The Physics of Supernovae, Springer-Verlag, Berlin, p200
Valenti S. et al., 2014, MNRAS, 438, L101
Valenti S. et al., 2015, MNRAS, 448, 2608
Valenti S. et al., 2016, MNRAS, 459, 3939
Van Dyk S. D., Li W., Filippenko A. V., 2003, PASP, 115, 1289
Verheijen M. A. W., Bershady M. A., Andersen D. R., Swaters R. A., Westfall K., Kelz A., Roth M. M., 2004, Astron. Nachr., 325, 151
Waxman E., Mészáros P., Campana S., 2007, ApJ, 667, 351
Weiler K. W., Sramek R. A., Panagia N., van der Hulst J. M., Salvati M., 1986, ApJ, 301, 790
Woosley S. E., Pinto P. A., Martin P. G., Weaver T. A., 1987, ApJ, 318, 664
Yaron O. et al., 2017, Nature Phys. 13, 510
Yuan F. et al., 2016, MNRAS, 461, 2003

This paper has been typeset from a TEX/LATEX file prepared by the author.